

RESEARCH ARTICLE Tracking gravity waves in moist baroclinic jet-front systems

10.1002/2014MS000395

Key Points:

- Ray-tracing experiments are performed to study gravity waves in moist flows
- Convection may force new waves and modify existing dry waves induced by jet
- Thermodynamics effect may counteract, enhance, or even take over wind effect

Correspondence to:

J. Wei,
jwei@psu.edu

Citation:

Wei, J., and F. Zhang (2015), Tracking gravity waves in moist baroclinic jet-front systems, *J. Adv. Model. Earth Syst.*, 07, doi:10.1002/2014MS000395.

Received 2 OCT 2014

Accepted 13 DEC 2014

Accepted article online 18 DEC 2014

Junhong Wei¹ and Fuqing Zhang¹

¹Department of Meteorology, Pennsylvania State University, University Park, Pennsylvania, USA

Abstract A series of four-dimensional ray-tracing experiments are performed to investigate the propagating wave characteristics, source mechanisms, and wave number vector refraction budget of six groups of lower-stratospheric gravity waves in the moist baroclinic jet-front systems with varying degree of convective instability. On one hand, the resemblance of ray trajectories and propagating characteristics between gravity waves in the dry experiment versus those in the experiment with weak diabatic heating demonstrates the limited role of moist convection in modifying those wave modes that are dominated by dry dynamics, including both the short-scale northward-propagating mode and the intermediate-scale northward-propagating mode in the jet exit region (likely induced by upper-level jet imbalance and/or tropospheric frontogenesis), the intermediate-scale eastward-propagating mode from the jet exit region in the ridge down to the jet entrance region in the trough (likely induced by upper-level jet imbalance), and the short-scale southward-propagating mode located far to the south of the jet right above the surface cold front (likely induced by tropospheric frontogenesis). On the other hand, comparisons of the gravity waves in the two aforementioned experiments through the ray tracing analysis further demonstrate that moist convection may force new wave modes, modify existing dry wave modes through latent heat release, or modify the new/existing waves through modification of large-scale flow. Convectively generated gravity waves could propagate both upstream and downstream of the latent heating. Lastly, it is indicated in the budget analysis of wave number vector refraction equations that the wind effect on changing the characteristics of propagating gravity waves generally dominates over the thermodynamics effect, and that the thermodynamics effect may counteract, enhance, or even take over the effect of background wind for those wave packets crossing the tropopause or frontal systems.

1. Introduction

As one of the most fundamental dynamical processes in meteorology, gravity waves, essentially buoyancy oscillations that may be influenced by the earth's rotation, are closely associated with a wide variety of atmospheric processes. The sources of excited gravity waves include topographic forcing, density impulses, convection, shear instability, geostrophic adjustment related to jets, fronts, and strong diabatic heating [Hooke, 1986; Fritts and Alexander, 2003; Kim *et al.*, 2003]. A better understanding of their origin and evolution, as well as their characteristic properties and the momentum flux they carry from source to sink, remains a great challenge.

Atmospheric jets are known to generate gravity waves [Plougonven and Zhang, 2014]. Many studies have documented the generation and propagation of gravity waves associated with the baroclinic jet-front system, including those based on observational tools [e.g., Uccellini and Koch, 1987; Bosart *et al.*, 1998], numerical investigations of the observed cases [e.g., Zhang and Koch, 2000; Zhang *et al.*, 2001; Koch *et al.*, 2001; Zhang *et al.*, 2003; Wu and Zhang, 2004; Zhang *et al.*, 2013], and the idealized simulations of baroclinic waves [e.g., O'Sullivan and Dunkerton, 1995; Zhang, 2004, hereinafter Z04; Wang and Zhang, 2007; Plougonven and Snyder, 2007; Lin and Zhang, 2008, hereinafter LZ08] and vortex dipole [e.g., Snyder *et al.*, 2007, 2009; Wang *et al.*, 2009, 2010; Wang and Zhang, 2010]. Among the above mentioned studies, Z04 applied 3.3 km high-resolution mesoscale numerical simulation and successfully reproduced gravity waves with horizontal wavelength about 100–200 km in the jet exit region during the life cycle of idealized baroclinic waves. He further proposed that balance adjustment, as a generalization of geostrophic adjustment [e.g., Rossby, 1938; Cahn, 1945; Blumen, 1972], is responsible for gravity wave generation in the jet in which gravity waves are continuously forced by flow imbalance while the developing background baroclinic waves are continuously producing flow imbalance that needs to be adjusted.

Frontal systems, including low-level and upper-level frontogenesis, are another significant contributor to the generation of gravity waves in the baroclinic jet-front systems [Plougonven and Zhang, 2014]. Snyder

This is an open access article under the terms of the Creative Commons Attribution-NonCommercial-NoDerivs License, which permits use and distribution in any medium, provided the original work is properly cited, the use is non-commercial and no modifications or adaptations are made.

et al. [1993] demonstrated with enhanced resolution and better initialization in idealized models that gravity waves with horizontal scales of 100–200 km can be emitted probably by frontogenesis when the advective timescale, which decreases as the cross-front scale was shortened dramatically, was comparable to or shorter than the inertial period. Also, another idealized simulation study in *Griffiths and Reeder* [1996], who considered a domain including a stratosphere, suggested that low-frequency gravity waves with horizontal wavelengths of order 400–1200 km can be generated from upper-level frontogenesis and propagate up into the stratosphere. In addition, their models revealed that the emitted gravity wave amplitude was mostly determined by the rapidity of the frontogenesis rather than intensity.

Moist convection is also closely linked with gravity waves in the jet-front baroclinic wave [e.g., *Koch and Dorian*, 1988; *Zhang and Fritsch*, 1988; *Powers*, 1997; *Bosart et al.*, 1998; *Zhang et al.*, 2001; *Lane and Reeder*, 2001; *Jewett et al.*, 2003]. On one hand, as a time-varying thermal forcing that interacts with the overlying stable layer and shear, moist convection itself can be an important source of gravity waves [e.g., *Clark et al.*, 1986; *Fovell et al.*, 1992; *Alexander et al.*, 1995]. On the other hand, moist convection may have an important impact on the evolution of the baroclinic waves and jet imbalance [e.g., *Gutowski et al.*, 1992]. However, most past idealized baroclinic wave experiments on gravity wave dynamics were primarily based on dry atmospheric models [e.g., *Wang and Zhang*, 2007; *Plougonven and Snyder*, 2007; OD95; Z04], which excluded the existence of moist convection as an active and significant contributor to both gravity waves and baroclinic waves. As an extension of the dry dynamics in Z04 and *Wang and Zhang* [2007], *Wei and Zhang* [2014, hereinafter WZ14] recently performed a series of cloud-permitting simulations to study the characteristics of mesoscale gravity waves in the moist baroclinic jet-front systems with varying degree of convective instability, and they demonstrated a much more energetic gravity wavefield with increasingly higher initial moisture content (also see section 3). Meanwhile, the impact of moisture on gravity wave generation was also assessed by *Mirzaei et al.* [2014], who proposed an empirical parameterization scheme for gravity wave energy based on the fast large-scale ageostrophic flow associated with the jet, front, and convection.

The ray tracing technique [*Lighthill*, 1978; *Büehler*, 2009; *Aspden and Vanneste*, 2010] has been widely used as a common approach to trace emitted gravity waves or to identify their sources in both observed cases [e.g., *Guest et al.*, 2000; *Hertzog et al.*, 2001; *Gerrard et al.*, 2004] and idealized simulations [e.g., *Reeder and Griffiths*, 1996; LZ08], and to investigate the influence of the complex flows on wave characteristics (e.g., wavelength, frequency, phase speed, group speed, and direction) by following their propagations along the ray trajectories [e.g., *Jones*, 1969; *Dunkerton and Butchart*, 1984; *Wang et al.*, 2009, 2010]. With the additional help of two-dimensional spectral decomposition, the ray tracing analysis in LZ08 for the dry idealized baroclinic waves in Z04 revealed strikingly different behaviors of gravity waves with different wavelengths (e.g., the shorter scale, the medium scale) from different origins (e.g., fronts, jets), and they also demonstrated the strong sensitivity of gravity wave characteristics to the spatial and temporal variability of the four-dimensional varying background atmosphere. *Wang et al.* [2009] employed the ray tracing technique to evaluate the possibility of wave capture mechanism [*Badulin and Shrira*, 1993; *Büehler and McIntyre*, 2005; *Plougonven and Snyder*, 2005] for the jet exit region gravity waves in the idealized vortex dipole with simple structure and slowly evolving nature. Subsequent study in *Wang et al.* [2010] suggested that the horizontal and vertical shears constrained rays along the dipole axis to be focused to the vicinity where the line of constant shear aspect ratio approximated to the characteristic large-scale environmental aspect ratio.

The purpose of the present paper is threefold. First, the simulated gravity wave characteristics in moist baroclinic jet-front systems by WZ14 will be summarized and reexamined using a two-dimensional Fourier decomposition method. Second, a potential source mechanism for the simulated waves will be identified based on a four-dimensional ray tracing numerical model. Third, the influence of the propagating media on wave characteristics, as well as on the ray trajectories, will be investigated. This research can be viewed as the counterpart of the earlier work of LZ08 on tracking wave events in dry baroclinic jet-front systems by Z04.

The present article is arranged as follows. A brief introduction to the ray-tracing model and background data resources for the work will be presented in section 2, followed in section 3 by an overview of the characteristics of gravity waves simulated in WZ14. Section 4 will present the results of ray tracing analysis for the gravity waves. The analysis of propagation effect for the simulated gravity waves, as well as their budget analysis of wave number vector refraction, will be explored in section 5. Section 6 contains a summary and discussion.

2. Experimental Design

2.1. The Ray-Tracing Model

The Gravity Wave Regional or Global Tracer (GROGRAT) model, a ray-tracing model that tracks the propagation and amplitude evolution of gravity waves, is employed in this study. Based on the core Wentzel-Kramers-Brillouin (WKB) ray tracing formalism (i.e., equations (A5a)–(A5f) in Appendix A) [Marks and Eckermann, 1995] described the theory and computational implementation of the first generation of GROGRAT. Eckermann and Marks [1996, 1997] have since upgraded GROGRAT to the next generation. GROGRAT incorporates the four-dimensional rotating stratified compressible flow and accommodates the nonhydrostatic gravity waves of all frequencies. Originally designed for global models, GROGRAT was also modified for calculations on an f-plane and for mesoscale models as in LZ08 and Wang *et al.* [2009, 2010].

2.2. Background Atmosphere Used in the Ray-Tracing Model

The gridded numerical representation of the background atmosphere (e.g., u , v , w , N^2 , and α^2 in equations (A5a)–(A5f)) ingested into GROGRAT comes from the mesoscale models in WZ14 (details in section 3). To account for the four-dimensional (time and space) background variations in the ray tracing, the simulated data are available every 3 h for GROGRAT. To overcome the computational memory issue, the model output is coarsened to 30 km (0.5 km) horizontal (vertical) grids. To avoid violation of standard asymptotic WKB assumptions, a low-pass filter [e.g., Wang and Zhang, 2007; Zhang *et al.*, 2007; LZ08; WZ14] is further applied to extract large-scale background flow with horizontal wavelength over 600 km. In addition, a Coriolis parameter $f = 10^{-4}$ rad/s is used.

2.3. Initial Condition in the Ray Integration and Its Termination

The direct input parameters for GROGRAT include the initial position of ray (x_0, y_0, z_0) or \vec{X}_0 , the initial time t_0 , the initial horizontal wave number vector (k_0, l_0) or \vec{K}_{H0} , the initial absolute frequency ω_0 , and the initial peak horizontal velocity amplitude along the horizontal wave number vector (not discussed in the current study). The magnitude of \vec{K}_{H0} is given by $|\vec{K}_{H0}| = \sqrt{(k_0^2 + l_0^2)} = \frac{2\pi}{\lambda_{H0}}$, where λ_{H0} is the initial horizontal wavelength identified with the additional help of the two-dimensional spectral decomposition. The magnitude of the initial absolute frequency ω_0 is given by $|\omega_0| = |\vec{K}_{H0}| \cdot |\vec{c}_{p0}|$, where \vec{c}_{p0} is the ground-based phase speed over a 2 h period centered on the selected time when $t = t_0$. All the other parameters can be achieved based on linear theory from the direct input parameters and background atmosphere.

Table 1 lists the potential scenario that the tracing experiment may stop. First, ray integration will be terminated immediately if any of the conditions in the scenarios A–D of Table 1 is satisfied. Second, unlike LZ08, the current study will still proceed with the integration even if WKB assumption may be violated (i.e., scenario E in Table 1), but those cases will be highlighted or justified in the discussion (also see the 10th column in Tables 2 and 3). Third, the integration may also be ended manually (i.e., scenario F in Table 1) if the ray propagates into an irrelevant region (or an unrelated temporal stage) or any other reason mentioned in the discussion.

3. Overview of Gravity Waves Simulated in WZ14

This study attempts to understand the source mechanisms and characteristics of the gravity waves initiated from the developing moist baroclinic jet-front systems in the high-resolution mesoscale models of WZ14 (10 km horizontal grid spacing and ~ 300 m vertical grid spacing on average). The idealized numerical experiments in WZ14 employ the Advanced Research version of the Weather Research and Forecast (WRF-ARW) model [Skamarock *et al.*, 2008] version 3.4. The simulations are performed in an f-plane rectangular channel with 4000 km (8020 km; 22 km) in x (y ; z) direction. The channel has periodic boundary conditions in x direction, and rigid boundaries (symmetric boundary conditions) in y direction. Rayleigh damping [Klemp *et al.*, 2008] is employed for the top 5 km. Lin *et al.* [1983] microphysics scheme is selected for moist processes, and convection scheme is turned off. Surface fluxes, friction, and radiation are all neglected.

The initial conditions of the idealized moist mesoscale simulations in WZ14 consist of a baroclinically unstable jet and specified relative humidity fields with different degree. The initial idealized baroclinic jet is the superposition of a simplified two-dimensional balanced zonal jet and its most unstable normal mode with a 4000 km zonal wavelength [also see Simmons and Hoskins, 1978; Wang and Zhang, 2007; Z04]. With the same initial idealized baroclinic jet, a dry experiment and a full moist experiment are performed, which are called EXP00

Table 1. Categories of Ray Terminations, Including the Code Names Used in Tables 2 and 3, Their Scenario That the Ray Integration Stops, and Detailed Descriptions

Code Name	Scenario	Code and Description
A	Ray reaches the time limit or boundary of the physical domain	A.1) Ray passes model top at 22.0 km A.2) Ray passes below 0.5 km A.3) Ray outside time range
B	Ray stalls vertically	B.1) The absolute value of vertical group velocity $ c_{gz} $ falls below 0.01 ms^{-1}
C	Inertial critical level	C.1) The absolute value of intrinsic frequency reaches Coriolis parameter (i.e., $ \Omega = f$)
D	Evanescent wave	D.1) The initial absolute vertical wave number is too small
E	The Wentzel-Kramers-Brillouin (WKB) conditions are violated	E.1) WKB breaks down in z-direction (i.e., $\delta_z = \frac{1}{m^2} \left \frac{\partial m}{\partial z} \right \approx \left \frac{1}{c_{gz} m^2} \frac{dm}{dt} \right \geq 1$; also see <i>Broutman</i> [1984] and <i>Marks and Eckermann</i> [1995])
F	Ray is terminated manually	F.1) Ray propagates into an irrelevant region F.2) Ray propagates into an unrelated temporal stage F.3) Ray propagates with weak vertical group velocity for a long time

and EXP100, respectively. The initial relative humidity field in EXP100 refers to the corrigendum [Tan et al., 2008] for Tan et al. [2004]. Several additional experiments (EXP80, EXP60, EXP40, and EXP20) reducing the initial relative humidity to 80, 60, 40, and 20% of that in EXP100 are also performed. In other words, the numbers 00–100 in each experiment (i.e., EXP00–EXP100) represent the percentages of a reference relative humidity profile.

Figure 1 demonstrates and compares the general behaviors of large-scale structures (1 km temperature, 8 km horizontal wind, and 7 km dynamic tropopause) and gravity wave signals (12 km horizontal divergence) among six baroclinic wave simulations (i.e., EXP00–EXP100) at selected times when all the experiments share similar amplitudes of synoptic-scale atmospheric wind perturbations (also when the mature jet exit gravity waves emerge in EXP00). It is found that the larger the initial moisture content, the faster the growth rates of both baroclinic wave component and gravity wave component. Figure 1 also suggests much more gravity wave signals with increasingly higher initial moisture content (e.g., much more red/blue contour lines in Figures 1d–1f than those in Figures 1a–1c), when comparing simulations with similar baroclinic wave patterns. In particular, the dry experiment with no moisture in EXP00 (Figure 1a) reproduces all the five gravity wave modes (WP1–WP5 marked in Figure 1a) simulated in Z04. Under weak convective instability with small amount of moisture in EXP20 (Figure 1b), dry dynamic gravity wave modes continue to dominate. However, a potentially new convective gravity wave mode (WP6; not shown in Figure 1) is observed ~ 30 h before dry gravity wave modes become mature. For gravity wave upstream of the convection, the wave locations and the gravity wave characteristics (WP3 marked in Figure 1b) are somewhat modified. For gravity wave downstream of the convection, the amplitudes of the waves (WP5 marked in Figure 1b) are noticeably enhanced. Under enhanced but still moderate convective instability in EXP40 (Figure 1c) and EXP60 (Figure 1d), both shorter-scale waves and intermediate-scale waves are essential to the lower-stratosphere divergence. Under strong convective instability in EXP80 (Figure 1e) and EXP100 (Figure 1f), the lower-stratosphere divergence manifests shorter-scale wave signatures filling the whole region of the baroclinic jet, instead of behaving as localized wave packets like those in EXP00 (Figure 1a) and EXP20 (Figure 1b).

The gravity wave characteristics for the six highlighted gravity wave modes (i.e., WP1–WP6) in EXP00, EXP20, and EXP100 are listed in Table 1 of WZ14, although characterizations of each of the many other modes of gravity waves existed in full or other moist experiments are not documented in detail. Two hypotheses are proposed in WZ14 to explain the partial enhancements or partial modifications of some particular wave modes in EXP20 (relative to EXP00). The first hypothesis is based on the generation effect associated with enhanced localized baroclinic instability; the other one relies on the propagation effect associated with background flow.

It is still unknown about the importance or the limitation of moisture for the six highlighted gravity wave modes (i.e., WP1–WP6) in EXP00, EXP20, and EXP100 of WZ14. Thus, the ray tracing techniques are employed to re-examine the source mechanism study in LZ08 and evaluate the hypotheses in WZ14, and particularly to differentiate the wave tracking analysis in EXP20 from that in EXP00 based on GROGRAT.

4. Ray Tracing Analysis and Source Mechanisms

4.1. WP1-EXP00 Versus WP1-EXP20: The Shorter-Scale Wave Packets in the Jet-Exit Region

Figure 2 shows the first two gravity wave modes (WP1 and WP2; also marked in Figures 1a–1b) in EXP00 and EXP20, which include the northward-propagating shorter-scale and intermediate-scale wave packets pronounced in the exit region of the upper-tropospheric jet. Similar to LZ08 (their Figure 2), the divergence

Table 2. Parameters of Named Ray Integrations and Their Termination Reasons (the Selected Rays in This Table Demonstrate the Limited Role of Moisture in Modifying Dry Gravity Wave Modes)^a

Ray Integrations	λ_H (km)	ϕ (°)	$ \vec{c}_{pH} $ (ms ⁻¹)	H (km)	t (h)	c_{gz} (ms ⁻¹)	λ_Z (km)	Ω (10 ⁻⁴ s ⁻¹)	Termination Reason
WP1-EXP00-N	90.0	84.3	4.6	12.0	132.0	0.078	1.5	3.5	B.1
	458.0	-5.7	8.2	0.7	112.0	0.010	0.9	1.0	
WP1-EXP00-C	90.0	84.3	4.6	12.0	132.0	0.086	1.5	3.7	A.2
	287.0	23.3	9.3	0.5	120.3	0.017	1.3	1.1	
WP1-EXP00-S	90.0	84.3	4.6	12.0	132.0	NA	1.7	NA	A.2
	154.7	55.6	10.6	0.4	125.3	0.102	3.9	1.9	
WP1-EXP20-N	82.5	84.3	4.7	12.0	132.0	0.087	1.5	3.8	B.1
	420.6	9.1	6.6	0.5	116.6	0.010	0.6	1.0	
WP1-EXP20-C	82.5	84.3	4.7	12.0	132.0	0.095	1.5	4.0	A.2
	266.7	29.9	12.3	0.5	121.6	0.019	1.2	1.1	
WP1-EXP20-S	82.5	84.3	4.7	12.0	132.0	NA	1.7	NA	A.2
	179.5	51.9	14.1	0.5	124.9	0.032	1.8	1.3	
WP2-EXP00-N	310.0	71.0	6.9	12.0	132.0	0.065	2.5	2.0	B.1
	756.3	23.7	6.5	1.6	103.4	0.010	1.3	1.0	
WP2-EXP00-C	310.0	71.0	6.9	12.0	132.0	0.086	2.8	2.2	A.2
	1312.5	57.6	4.5	0.5	113.6	0.012	3.3	1.1	
WP2-EXP00-S	310.0	71.0	6.9	12.0	132.0	NA	2.8	NA	A.2
	310.0	71.0	6.9	12.0	132.0	0.111	3.2	2.5	
WP2-EXP20-N	298.1	50.8	8.5	0.3	125.6	0.263	8.5	2.3	B.1
	310.0	71.0	6.9	12.0	132.0	0.067	2.5	2.0	
WP2-EXP20-C	735.6	32.7	5.7	1.4	103.0	0.009	1.4	1.0	A.2
	310.0	71.0	6.9	12.0	132.0	0.087	2.9	2.2	
WP2-EXP20-S	1421.4	59.4	6.7	0.5	112.9	0.010	3.0	1.0	A.2
	310.0	71.0	6.9	12.0	132.0	NA	2.8	NA	
WP4-EXP00-N	310.0	71.0	6.9	12.0	132.0	0.116	3.3	2.5	A.2
	307.8	49.7	9.5	0.5	125.8	0.237	8.4	2.2	
WP4-EXP00-C	96.0	-82.9	6.8	10.0	132.0	0.070	2.0	2.6	B.1
	194.0	-89.3	6.5	3.7	80.8	0.010	1.3	1.3	
WP4-EXP00-S	96.0	-82.9	6.8	10.0	132.0	0.076	2.1	2.7	B.1
	182.0	87.5	5.3	3.2	83.2	0.010	1.2	1.3	
WP4-EXP20-N	96.0	-82.9	6.8	10.0	132.0	NA	2.0	NA	B.1
	176.0	84.2	4.1	2.4	84.6	0.010	1.1	1.3	
WP4-EXP20-C	93.5	-82.9	7.1	10.0	132.0	0.081	2.1	2.7	B.1
	193.3	-89.3	6.6	3.2	84.6	0.010	1.3	1.3	
WP4-EXP20-S	93.5	-82.9	7.1	10.0	132.0	0.087	2.2	2.8	B.1
	172.9	89.5	6.2	3.1	89.0	0.010	1.2	1.4	
WP4-EXP20-S	93.5	-82.9	7.1	10.0	132.0	NA	2.0	NA	B.1
	171.8	88.1	5.7	2.3	90.7	0.010	1.2	1.4	

^aColumn 1–10 represent the names of the ray integrations, their horizontal wavelengths λ_H , horizontal wave vector angles ϕ in polar coordinate system, ground-based horizontal phase speeds $|\vec{c}_{pH}|$, heights H , ray times t , ground-based vertical group velocities c_{gz} , vertical wavelengths λ_Z , intrinsic frequencies Ω , and termination reasons (codes refer to Table 1). The first figures represent the starting values or initial direct input parameters. The second figures represent the ending values of the ray integrations. The third figures in the center ray experiments represent the observed values based on the simulation of WZ14. Ray integrations still proceed even if WKB assumption may be violated, but types of violations and their associated heights are given in column 10.

field is decomposed into the shorter-scale components with wavelengths between 50 and 200 km, and the intermediate-scale components with wavelengths between 200 and 600 km. WP1-EXP00 (WP1-EXP20) in Figure 2a (Figure 2b) represents the shorter-scale wave packets on the left side of the immediate jet exit region in EXP00 (EXP20). WP2-EXP00 (WP2-EXP20) in Figure 2c (Figure 2d) represents the intermediate-scale wave packets in the immediate exit region of the jet streak in EXP00 (EXP20). Even though WP1 and WP2 may share similar location and background flow at 12 km, they have distinctively different wave characteristics (also see Table 1 in WZ14). The ray tracing analysis of WP2 refers to section 4.2.

For the source mechanism study of an upward propagating wave packet such as WP1-EXP00, the tracing model is integrated backward in time and downward in altitude (also called reverse ray tracing or backtracing) from the observed time and height (e.g., 132 h and 12 km for WP1-EXP00). Three rays are initiated at different locations (north ray, green; center ray, blue; south ray, red). The direct input parameters for the center ray, including its positions and wave characteristics, are estimated at the starting point of the center

Table 3. Same as Table 2^a

Ray Integrations	λ_H (km)	ϕ (°)	$ \overrightarrow{c_{pH}} $ (ms ⁻¹)	H (km)	t (h)	c_{gz} (ms ⁻¹)	λ_Z (km)	Ω (10 ⁻⁴ s ⁻¹)	Termination Reason
WP3-EXP00-N	80.0	43.5	5.7	12.0	132.0	1.404	6.1	14.6	A.2
	75.3	-13.1	10.4	0.7	128.1	1.847	13.7	9.0	
WP3-EXP00-C	80.0	43.5	5.7	12.0	132.0	1.415	6.2	14.7	A.2
	71.1	-7.6	10.3	0.8	128.2	1.415	10.7	8.8	
WP3-EXP00-S	80.0	43.5	5.7	12.0	132.0	NA	6.2	NA	A.2
	80.0	43.5	5.7	12.0	132.0	1.432	6.2	14.9	
WP3a-EXP20-N	66.6	-6.0	10.2	0.6	128.2	1.195	8.8	8.9	A.2
	68.0	72.5	0.8	12.0	132.0	0.972	4.7	13.3	
WP3a-EXP20-C	73.1	12.1	10.2	0.4	128.1	0.934	8.5	7.2	A.2 (E.1 within 1.6-1.1 km)
	68.0	72.5	0.8	12.0	132.0	0.985	4.7	13.4	
WP3a-EXP20-S	64.0	16.4	9.9	0.4	128.2	0.488	4.9	6.6	A.2 (E.1 within 1.5-0.5 km)
	68.0	72.5	0.8	12.0	132.0	NA	4.9	NA	
WP3b-EXP20-N	68.0	72.5	0.8	12.0	132.0	0.993	4.7	13.5	A.2 (E.1 within 1.5-0.5 km)
	62.7	17.2	9.6	0.4	128.3	0.433	4.3	6.7	
WP3b-EXP20-C	108.0	24.2	7.9	12.0	132.0	0.956	5.8	10.6	B.1
	168.5	-23.8	7.7	5.6	122.2	0.010	1.1	1.4	
WP3b-EXP20-S	108.0	24.2	7.9	12.0	132.0	0.984	5.9	10.7	F.3
	248.3	-41.0	0.4	3.2	109.0	0.024	1.8	1.3	
WP3b-EXP20-S	108.0	24.2	7.9	12.0	132.0	NA	6.1	NA	F.3
	157.7	-55.5	0.8	2.9	110.9	0.020	1.3	1.4	
WP5s-EXP00-N	490.1	58.3	8.3	12.0	132.0	0.006	1.1	1.1	B.1
	490.1	58.3	8.3	12.0	131.9	0.006	1.1	1.1	
WP5s-EXP00-C	490.1	58.3	8.3	12.0	132.0	0.021	1.8	1.4	F.2
	1413.6	12.6	5.4	1.5	94.2	0.012	2.6	1.0	
WP5s-EXP00-S	490.1	58.3	8.3	12.0	132.0	NA	1.4	NA	B.1
	490.1	58.3	8.3	12.0	132.0	0.026	2.0	1.4	
WP5n-EXP00-N	159.8	55.5	4.3	0.9	107.9	0.010	1.5	1.4	B.1
	90.0	54.5	7.6	12.0	132.0	0.079	1.5	3.6	
WP5n-EXP00-C	410.7	47.9	5.0	6.8	103.8	0.009	1.3	1.3	B.1
	90.0	54.5	7.6	12.0	132.0	0.085	1.6	3.7	
WP5n-EXP00-S	527.1	45.7	2.0	6.3	103.6	0.007	1.6	1.2	B.1
	90.0	54.5	7.6	12.0	132.0	NA	1.6	NA	
WP5s-EXP20-N	90.0	54.5	7.6	12.0	132.0	0.105	1.7	4.1	B.1
	353.3	70.5	2.0	5.1	111.2	0.009	2.0	1.3	
WP5s-EXP20-C	450.0	58.3	9.0	12.0	132.0	0.012	1.3	1.2	F.1
	1412.7	36.9	4.8	10.0	107.4	0.036	5.2	1.2	
WP5s-EXP20-S	450.0	58.3	9.0	12.0	132.0	0.023	1.7	1.4	A.2
	1921.9	64.6	19.4	0.4	110.4	0.045	8.6	1.1	
WP5n-EXP20-N	450.0	58.3	9.0	12.0	132.0	NA	1.7	NA	B.1
	450.0	58.3	9.0	12.0	132.0	0.026	2.0	1.5	
WP5n-EXP20-C	149.2	66.0	3.0	1.0	110.3	0.009	1.4	1.5	F.2
	68.0	54.5	10.4	12.0	132.0	0.032	0.8	2.8	
WP5n-EXP20-S	194.4	-11.9	17.6	5.6	95.2	0.018	1.3	1.2	F.2
	68.0	54.5	10.4	12.0	132.0	0.039	0.9	3.0	
WP6-EXP20-N	213.8	-16.3	17.9	5.2	95.8	0.014	0.8	1.1	F.2
	68.0	54.5	10.4	12.0	132.0	NA	1.1	NA	
WP6-EXP20-C	68.0	54.5	10.4	12.0	132.0	0.049	1.0	3.3	B.1
	349.0	57.0	10.2	5.0	108.9	0.010	1.4	1.1	
WP6-EXP20-S	62.0	75.1	2.4	12.0	110.0	0.373	2.7	8.9	B.1
	102.0	54.8	3.5	0.9	98.6	0.010	0.7	1.4	
WP6-EXP100-N	62.0	75.1	2.4	12.0	110.0	0.388	2.7	9.0	B.1
	102.9	54.3	3.4	0.7	99.1	0.010	0.7	1.4	
WP6-EXP100-C	62.0	75.1	2.4	12.0	110.0	NA	2.8	NA	B.1
	62.0	75.1	2.4	12.0	110.0	0.402	2.8	9.2	
WP6-EXP100-S	104.8	53.7	3.2	0.6	99.4	0.010	0.7	1.4	B.1
	50.0	68.2	6.2	12.0	72.0	0.496	2.7	11.5	
WP6-EXP100-C	55.5	57.0	8.2	2.4	61.2	0.010	0.4	1.4	B.1
	50.0	68.2	6.2	12.0	72.0	0.512	2.8	11.8	
WP6-EXP100-S	53.6	57.7	8.0	2.3	61.3	0.010	0.4	1.4	B.1
	50.0	68.2	6.2	12.0	72.0	NA	2.9	NA	
WP6-EXP100-S	50.0	68.2	6.2	12.0	72.0	0.528	2.8	12.0	B.1
	52.0	58.4	7.9	2.3	61.4	0.010	0.4	1.5	

^aThe selected rays in this table suggest moist convection may force new wave modes, modify existing dry wave modes through latent heating release, or modify the new/existing waves through modification of large-scale flow.

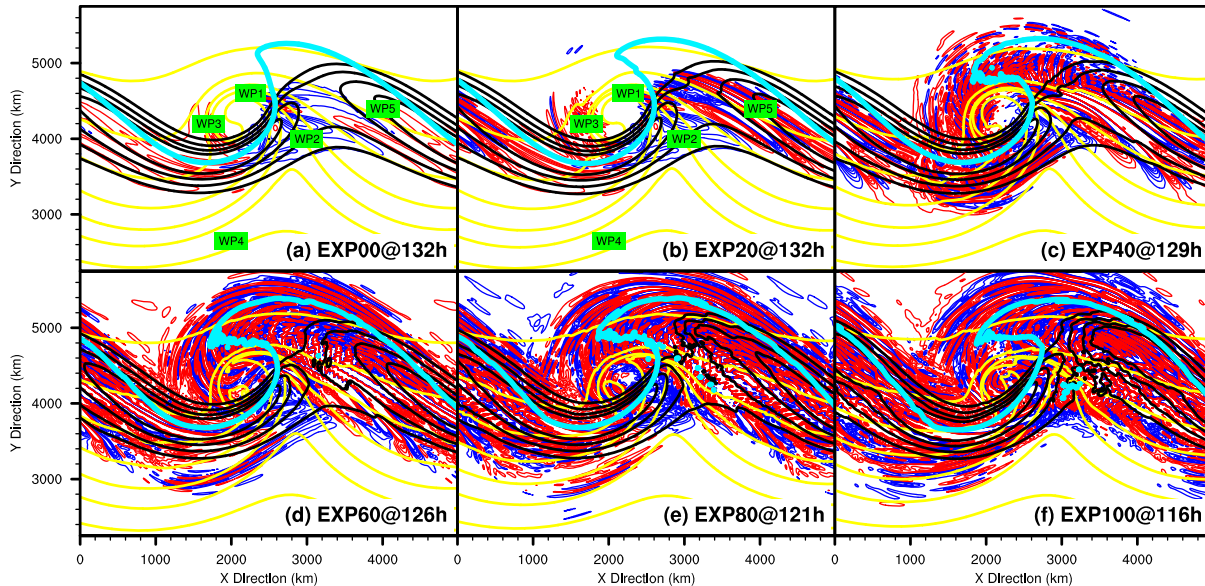


Figure 1. Simulated 1 km temperature (yellow lines; $\Delta = 5$ K), 8 km horizontal wind (black lines; contour levels at 40, 45, 50, and 55ms^{-1}), and 12 km horizontal divergence (blue lines, positive; red lines, negative; $\Delta = 2.0 \times 10^{-6}\text{s}^{-1}$; range within $\pm 1.2 \times 10^{-5}\text{s}^{-1}$; zero value omitted) in (a) EXP00 at 132 h, (b) EXP20 at 132 h, (c) EXP40 at 129 h, (d) EXP60 at 126 h, (e) EXP80 at 121 h, and (f) EXP100 at 116 h. The turquoise lines denote the 7 km dynamic tropopause where potential vorticity equals 1.5 PVU. WP1-WP5 are marked.

ray by measuring the four-dimensional simulations in WZ14 (also see section 2.3). The north ray and the south ray use the same direct input parameters of wave characteristics as those in the center ray, but their initial positions are different from each other by design. The observed initial wave vector directs from the starting point of the north ray to that of the south ray, and the distance between these two points represents the observed initial horizontal wavelength. The three ray experiments in WP1-EXP00 are called WP1-EXP00-N (north ray), WP1-EXP00-C (center ray), and WP1-EXP00-S (south ray), respectively. The other ray tracing experiments and their naming follow similar procedure.

Figures 2a–2b demonstrate a remarkable resemblance between WP1-EXP00 and WP1-EXP20 for the ray tracing trajectories in horizontal views. It is found that all the three rays for either WP1-EXP00 or WP1-EXP20 pass through the jet level, and they can be traced back to the surface level (ray integrations are stopped after rays pass below 1 km). Horizontally speaking, the south rays for both experiments maintain in the left side of the immediate jet exit region during the entire backtracing, but in contrast the center and north rays gradually migrate toward to right side below ~ 1.5 km. Particularly, there appears to be a turning point from the horizontal views for all the reverse ray tracing experiments within ~ 4.0 to ~ 8.0 km, where westward backtracing is succeeded by eastward backtracing.

Tables 2 and 3 list the initial conditions, final conditions of all the ray integrations (including WP1-EXP00 and WP1-EXP20 shown in Table 2) in the current research, as well as their termination reasons. It is suggested in Table 2 that the life times of all the three selected rays are different from each other, even though all of them are launched at the same time and height, and they can all be traced back to the surface level. For example, WP1-EXP00-S reaches the terminated height in a shorter period (6.7 h) than WP1-EXP00-C (11.7 h) and WP1-EXP00-N (20.0 h). Table 2 also indicates that the life times and termination reasons in WP1-EXP20 are substantially similar to those in WP1-EXP00.

Nine parameters are chosen to investigate the propagating wave characteristics along the rays, including horizontal wavelength λ_H , horizontal wave vector angle ϕ in polar coordinate system, vertical wavelength λ_Z , ground-based horizontal group velocity $|\vec{c}_{gH}|$, ground-based horizontal group velocity angle γ in polar coordinate system, ground-based vertical group velocity c_{gz} , intrinsic frequency Ω , angle δ between horizontal wave vector (k, l) and ground-based horizontal group velocity vector (c_{gx}, c_{gy}) , and ray time t . Here the angle ϕ is defined as $\phi = \frac{180}{\pi} \times \arctan \frac{l}{k}$ which ranges from -90° to 90° ; the angle γ is in the range between -180° and 180° ; the angle δ is confined to the range between 0° and 90° using the following equation:

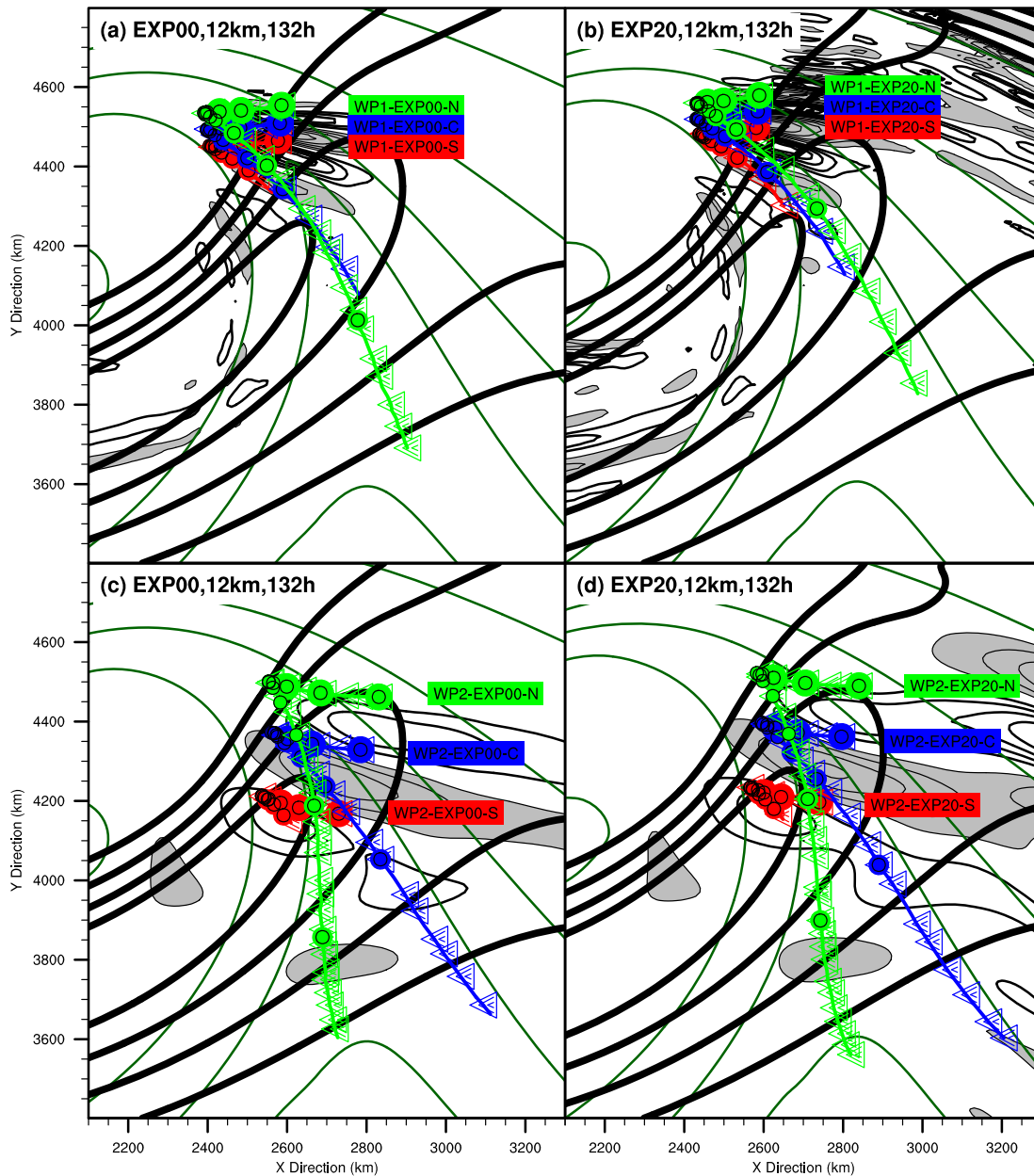


Figure 2. Horizontal views of three selected reverse ray tracing paths for (a, c) WP1-EXP00 and WP2-EXP00 in EXP00, (b, d) WP1-EXP20 and WP2-EXP20 in EXP20, overlapping on the corresponding 1 km temperature (dark green contours; $\Delta = 5$ K), 8 km horizontal wind (thick black contours; contour levels at 40, 45, 50, and 55ms^{-1}), and 12 km horizontal divergence (black contours; positive shaded; $\Delta = 2.0 \times 10^{-6} \text{s}^{-1}$; range within $\pm 1.2 \times 10^{-5} \text{s}^{-1}$; zero value omitted) in 132 h. (a, b) Shorter-scale divergence and (c, d) intermediate-scale divergence are used to separate WP1 and WP2. Raypath starting from south (center; north) point at 12 km in 132 h is shown in red (blue; green). Solid circles (triangles) represent ray positions approximately every 1 km (1 h), with large (medium; small) solid circles indicating levels 10–12 km (1–3; 4–9 km). Name of each ray integration is marked (also see ray parameters in Table 2 or Table 3). In order to show the relative position between the ray trajectories and the jet, the phase speed of the baroclinic wave ($\sim 13.9 \text{ms}^{-1}$) is subtracted from the local zonal ray speed.

$$\delta = 90 - \left| \frac{180}{\pi} \times \arctan\left(\frac{C_{gy}}{C_{gx}}\right) - \frac{180}{\pi} \times \arctan\left(\frac{l}{k}\right) - 90 \right|. \quad (1)$$

Note that if δ is close to 90° (0°), ray trajectories and horizontal phase lines tend to be parallel to (perpendicular to) each other in horizontal views, assuming that horizontal wave vectors and horizontal phase lines are perpendicular to each other.

Figures 3a–3i give the vertical profiles of the above mentioned nine selected parameters for WP1-EXP00 (three solid lines) and WP1-EXP20 (three dash lines), which continues to suggest that WP1-EXP00 and WP1-EXP20 share extremely similar life cycles and wave characteristics. It is worth mentioning that vertical

wavelengths λ_z appear to share rather similar vertical profiles with vertical group velocities c_{gz} and intrinsic frequencies Ω , despite the differences in their peak heights. In other words, large λ_z generally correspond to large c_{gz} and large Ω , and vice versa. Due to large c_{gz} between ~ 4.0 and ~ 8.0 km, their vertical propagations within this region are extremely fast (within ~ 1 h). This vertical region (~ 4.0 to ~ 8.0 km) also matches well with the turning point highlighted in the horizontal views of their ray tracing trajectories (Figures 2a and 2b), suggesting the contrast between propagating waves in lower stratosphere (~ 8.0 – 12.0 km) and those in lower troposphere (below ~ 4.0 km).

Next examined are the positions (x, y) and horizontal wave number (i.e., both horizontal wavelength λ_H and horizontal wave vector polar angle ϕ) of the GROGRAT-simulated rays at different levels and their projections onto WRF-simulated horizontal divergence fields at the closest integer hours to the times the center rays intercept the given levels (not shown). Despite the shifting in horizontal views, WP1-EXP00-C and WP1-EXP20-C generally coincide well with the shorter-wave signals from 12 km to jet level, tropopause level, then down to ~ 1.5 km (surface occluded fronts) based on WRF, covering almost their entire life cycles. Therefore, the wave energy source can be anywhere from ~ 1.5 to 12 km. This comparison between GROGRAT and WRF further confirms the conclusion in LZ08 that the potential source of WP1 in dry experiment (i.e., WP1-EXP00) may be the upper-tropospheric jet-front system and (or) the surface frontal system. Moreover, since experiment with small amount of moisture produces life cycles of WP1-EXP20 that are essentially the same as those of WP1-EXP00, both of them should originate from the same dry source.

4.2. WP2-EXP00 Versus WP2-EXP20: The Medium-Scale Wave Packets in the Jet-Exit Region

The resemblance in horizontal views of the ray tracing trajectories between WP2-EXP00 and WP2-EXP20 is also shown in Figures 2c and 2d. Similar to WP1, all of the three selected rays for WP2 can also be traced back to the surface level (also see Table 2). For the center and south rays, they stop at 0.5 km because they hit the bottom boundary. For the north rays, they stop at ~ 1.5 km due to weakening vertical group velocity, as wave packets approach inertial critical levels where the absolute value of intrinsic frequency equals to Coriolis parameter. The three-stage conceptual model in the horizontal views of WP1 can also be applied to WP2. Take the center rays as an example, the region from 12 to ~ 9.0 km corresponds to westward backtracing (the first stage); the region from ~ 9.0 to ~ 3.5 km corresponds to the turning point with no apparent horizontal shift (the second stage); the region below ~ 3.5 km corresponds to eastward backtracing (the third stage). Unlike WP1, the turning angles at the last stage noticeably differ from each other among three selected rays for WP2. Furthermore, Figures 3j–3r again illustrates that the vertical profiles of propagating wave characteristics between WP2-EXP00 (three solid lines) and WP2-EXP20 (three dash lines) are almost identical.

To understand the generation mechanism of WP2, Figure 4 demonstrates horizontal views of WP2-EXP00-C at nine selected levels of EXP00 during its reverse ray tracing. It is suggested in Figures 4a–4d that the position (x, y) , the horizontal wavelength λ_H , and the horizontal wave vector polar angle ϕ of WP2-EXP00-C from GROGRAT match the WRF-simulated horizontal divergence fields quite well from 12 to ~ 10.5 km (from 132 to ~ 129 h). However, there is noticeable discrepancy between GROGRAT and WRF at ~ 9.0 km (Figure 4e) which becomes more severe from ~ 7.5 to ~ 5.5 km (Figures 4f–4g). Such a sharp disagreement implies that the wave source may be somewhere above ~ 9.0 to ~ 7.5 km. Therefore, the potential source of WP2-EXP00 may be the upper-tropospheric jet-front system, which is consistent with what was found in LZ08. Judging from the similarity between WP2-EXP00 and WP2-EXP20 in Figures 2c and 2d and Figures 3j–3r, WP2-EXP20 should have the same wave source as WP2-EXP00.

The life cycles of WP1 (Figures 2a and 2b; Figures 3a–3i) and WP2 (Figures 2c and 2d; Figures 3j–3r) have many aspects in common. For example, the turning point in the second stage corresponds to the region with large c_{gz} ; also, the south (north) rays generally have largest (smallest) λ_z , c_{gz} , and Ω . Despite the resemblance, WP2 differs from WP1 in several key respects. First, the maxima of λ_H and λ_z in WP2 are larger than those in WP1. Second, the maxima of c_{gz} and Ω in WP2 are smaller than those in WP1. Third, the heights of the λ_z maxima in WP2 are slightly higher than those in WP1, so are the maxima heights of c_{gz} and Ω . Fourth, WP1 and WP2 may be generated by different wave sources at different heights.

4.3. WP3-EXP00 Versus WP3a-EXP20: The Shorter-Scale Wave Packets in the Deep Trough Region

Figures 5a and 5b show the examples of the third gravity wave mode (WP3; also marked in Figures 1a and 1b) highlighted in WZ14. WP3-EXP00 (Figure 5a) represents the shorter-scale wave packets over the deep

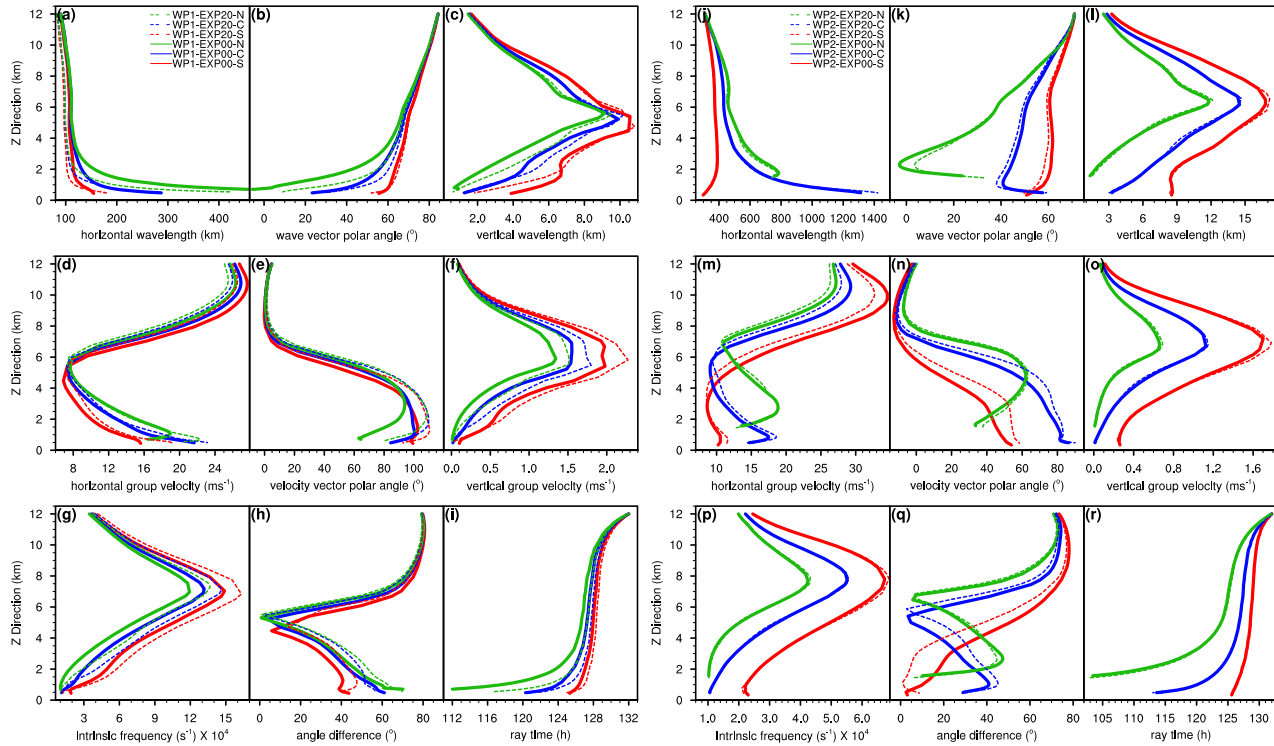


Figure 3. Vertical profiles of horizontal wavelength λ_H (km), horizontal wave vector angle ϕ ($^\circ$) in polar coordinate system, vertical wavelength λ_z (km), ground-based horizontal group velocity $|c_{gH}|$ (ms^{-1}), ground-based horizontal group velocity angle γ ($^\circ$) in polar coordinate system, ground-based vertical group velocity c_{gz} (ms^{-1}), intrinsic frequency Ω (s^{-1}) times 10^4 , angle δ ($^\circ$) between horizontal wave vector and ground-based horizontal group velocity vector (also see equation (1)), and ray time t (h) for selected backtraced rays from (a–i) WP1-EXP00 (solid lines) versus WP1-EXP20 (dash lines), and (j–r) WP2-EXP00 (solid lines) versus WP2-EXP20 (dash lines) during their backward and downward integrations.

trough region above the jet in EXP00, and WP3a-EXP20 (Figure 5b) represents those in EXP20. Both WP3-EXP00 and WP3a-EXP20 behave as bended shorter-scale wave packets almost parallel to the surface occluded front to the south of the cyclone center, and they share remarkably high intrinsic frequencies with 13–15 times the Coriolis parameter at 12 km. Another shorter-scale gravity wave mode in EXP20, marked as WP3b-EXP20 in Figure 5b, is also shown to the west of the cyclone center. The ray tracing analysis of WP3b-EXP20 will be further described in section 4.4.

For the horizontal views of the ray tracing trajectories in WP3-EXP00 (Figure 5a) and WP3a-EXP20 (Figure 5b), their tracks are generally along the 1 km isothermal, as well as their own phase lines at 12 km. Vertically speaking, all the rays can be traced back to the bottom of the domain within only 4 h (also see Table 3). Due to their fast vertical penetrations, the horizontal propagations are quite limited within a short distance.

Generally speaking, the vertical profiles of the propagating wave characteristics between WP3-EXP00 and WP3a-EXP20 are broadly similar (Figures 6a–6i). However, compared with the similarity in WP1 or WP2 between EXP00 and EXP20 (i.e., WP1-EXP00 versus WP1-EXP20, or WP2-EXP00 versus WP2-EXP20), there are some noticeable differences. First, Figures 5a and 5b and Table 3 suggest a fine distinction in the initial conditions of the reverse ray tracing between WP3-EXP00 and WP3a-EXP20, including their locations and wave characteristics. Second, the heights of the jet cores for the traces in WP3a-EXP20 are slightly lower than those in WP3-EXP00 (not shown), accompanied by stronger jet cores. Third, the heights of tropopause for the traces in WP3a-EXP20 are also slightly lower, accompanied by stronger occluded frontal system. Fourth, the maxima/minima of λ_z , c_{gz} , and Ω for the traces in WP3a-EXP20 are accordingly lower than those in WP3-EXP00 by ~ 0.5 to ~ 1.5 km.

Despite the differences between WP3-EXP00 and WP3a-EXP20, their GROGRAT-simulated positions and horizontal wave number agree well with WRF-simulated horizontal divergence fields for the entire backtracing. These results show that WP3-EXP00 and WP3a-EXP20 should share the same wave energy source, and they are both likely to originate from the surface occluded frontal systems (even though the surface occluded frontal systems may be locally modified/strengthened by the moist processes in EXP20 relative to EXP00).

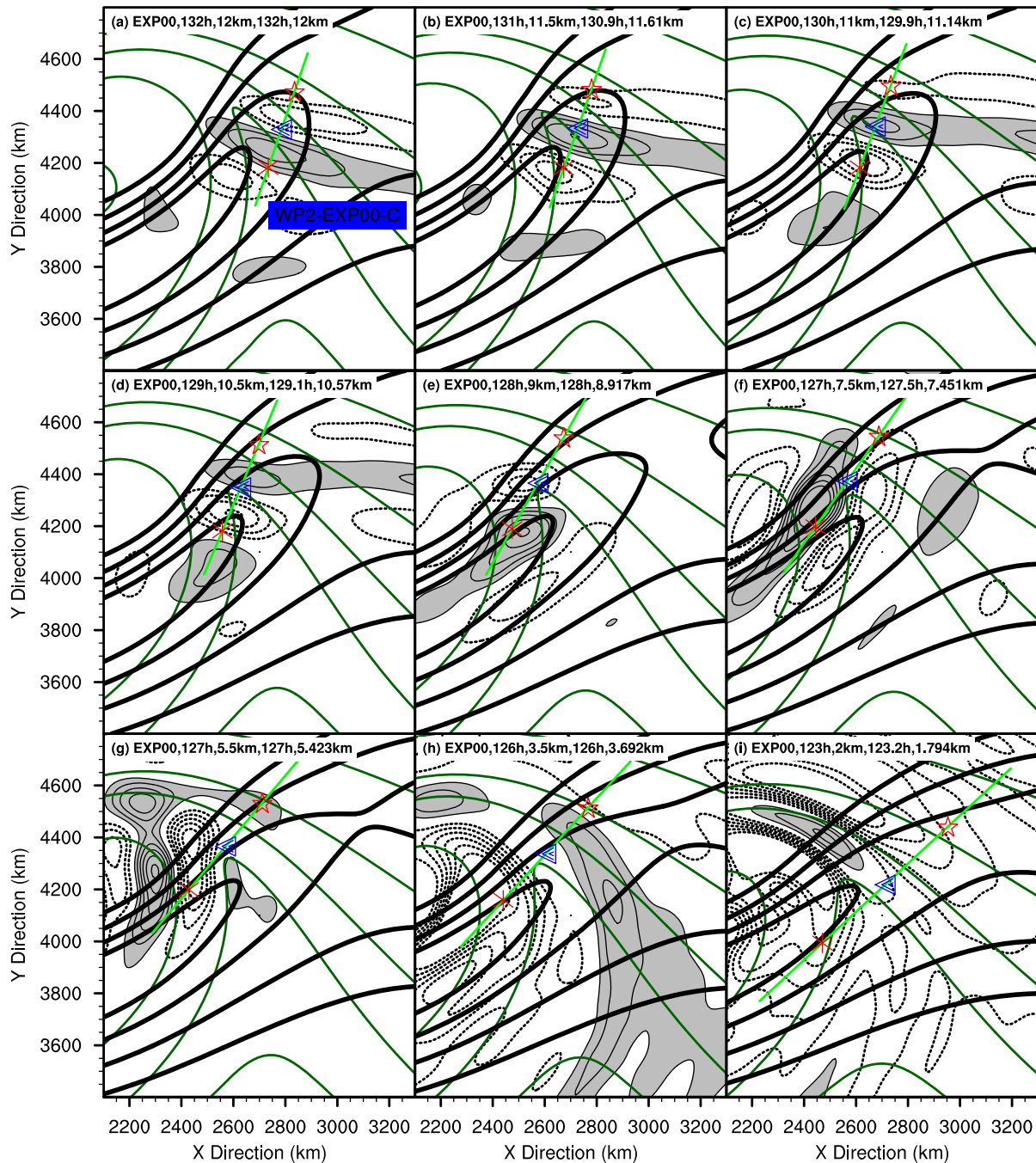


Figure 4. Horizontal views of WP2-EXP00-C in EXP00 at each selective time during its backward and downward integrations. Green lines (links between red marks) demonstrate distances of two (one) horizontal wavelength(s) and directions of horizontal wave vector during ray integration, with ray positions as the centers marked by blue triangles. Contours follow Figure 2, except that medium-scale horizontal divergence is used at closest available height level near the ray height. Top left subtitle in each subplot shows the label (a–i), name of WRF simulation, selected hour of simulated contours, height level of simulated horizontal divergence, ray time, ray height. Name of ray integration is marked in Figure 4a.

4.4. WP3b-EXP20: Additional Shorter-Scale Wave Packets to the West of the Cyclone Center

Compared to WP3a-EXP20, all the three selected rays for WP3b-EXP20 (Figure 5b) can be traced back to the far northeast of its initial position from 12 km down to 2.9–5.6 km (below the tropopause; also see Table 3). The vertical profiles of propagating wave characteristics in WP3b-EXP20 are given in Figures 6j–6r (three dashed lines). For all the three selected rays, there are no dramatic changes in horizontal wavelengths λ_H and vertical wavelengths λ_Z from ~ 12 to ~ 8 km. The propagations from ~ 12 to ~ 8 km are extremely fast (within ~ 1.5 h), which corresponds to relatively large c_{gz} . Generally speaking, from ~ 8 to ~ 6 km, the lower

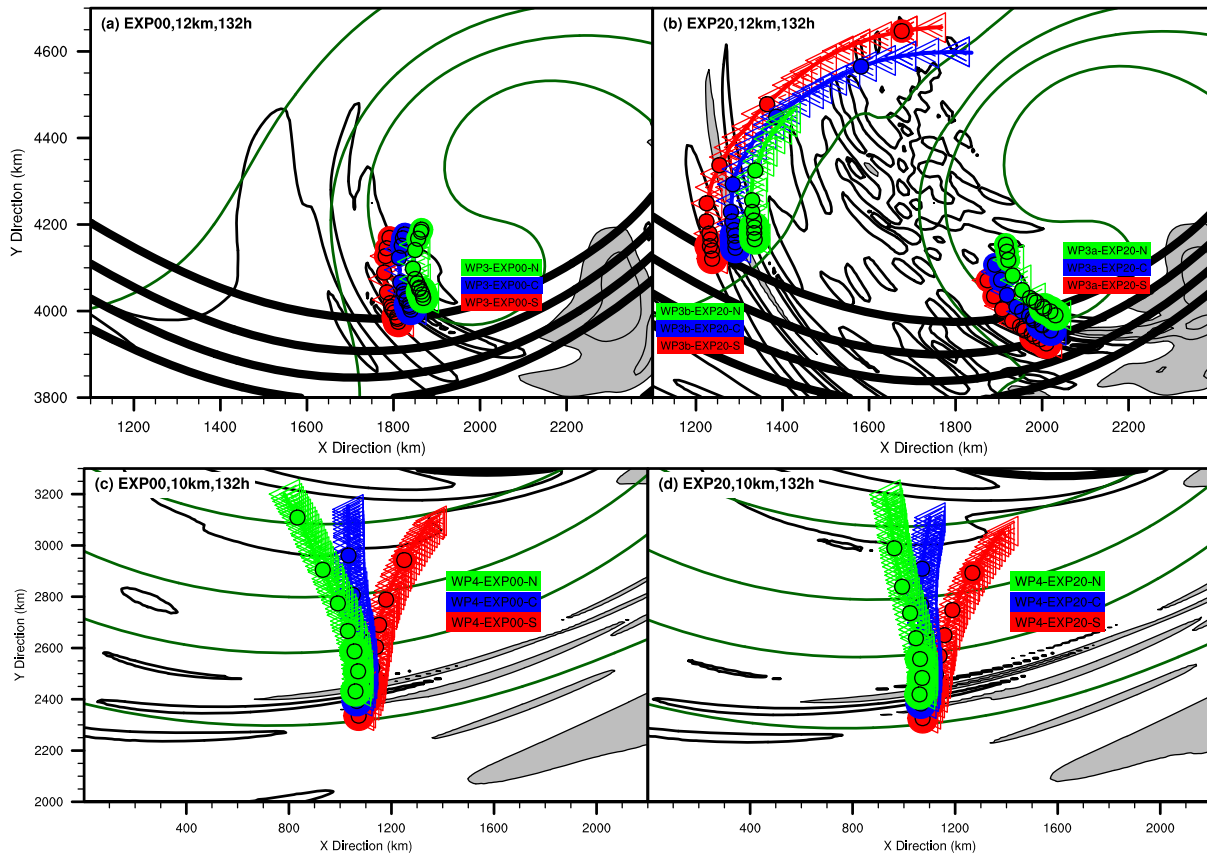


Figure 5. Same as Figure 2, but for (a) WP3-EXP00 in EXP00, (b) WP3a-EXP20 and WP3b-EXP20 in EXP20, (c) WP4-EXP00 in EXP00, and (d) WP4-EXP20 in EXP20. Twelve kilometer horizontal divergence (black contours; positive shaded; $\Delta = 2.0 \times 10^{-6} \text{ s}^{-1}$; range within $\pm 1.2 \times 10^{-5} \text{ s}^{-1}$; zero value omitted) is used in (a, b), and 10 km horizontal divergence (black contours; positive shaded; $\Delta = 1.0 \times 10^{-6} \text{ s}^{-1}$; range within $\pm 6.0 \times 10^{-6} \text{ s}^{-1}$; zero value omitted) is used in Figures 5c and 5d.

the rays are, the larger λ_H are, the smaller λ_Z are, the smaller c_{gz} and Ω are. Below ~ 6 km, c_{gz} are reducing to an extremely small value (e.g., 0.01 ms^{-1}), as WP3b-EXP20 appears to encounter the inertial critical level ($|\Omega| = f$).

Based on the horizontal views during the reverse ray tracing in Figure 7, it is suggested that WP3b-EXP20-C can be integrated backward to the edging area of the initial convective disturbance associated with latent heating release (the shaded color in Figure 7). For the nine selected levels in Figure 7, the position (x, y) and the horizontal wave vector polar angle ϕ from GRAGRAT match quite well with the bended horizontal divergence signals from WRF. Instead, the λ_H of GROGRAT and WRF agrees well with each other above the tropopause (~ 5 to ~ 6 km), but the GROGRAT-simulated λ_H is larger than the one simulated by WRF below the tropopause. This may be partially due to the difficulties in separating gravity waves and other dynamic processes in troposphere (e.g., moist convection and frontal circulation). The ray analysis in Figure 7 is consistent with the hypothesis in WZ14 that WP3b-EXP20 may be the result of escaping waves from the convection (also see the horizontal evolution of WP3b-EXP20 from 106 to 128 h in Figure 14 of WZ14), although one cannot completely rule out the contributions from the surface occluded frontal systems strengthened by the latent heating release.

Though substantially similar to WP3-EXP00 or WP3a-EXP20 observed at 12 km (e.g., shorter scale; bended phase lines; high Ω at 12 km), WP3b-EXP20 is distinguished in the following respects: first, due to its weak c_{gz} below ~ 8 km, WP3b-EXP20 has a much longer life cycle than either WP3-EXP00 or WP3a-EXP20 (~ 10 – 23 h versus ~ 4 h); second, WP3-EXP00 or WP3a-EXP20 maintains large c_{gz} and high Ω without reaching inertial critical levels during the backtracing, but WP3b-EXP20 exhibits rather small c_{gz} and low Ω at the end of the life cycles; third, the wave energy source of WP3b-EXP20 may be different from either WP3-EXP00 or WP3a-EXP20.

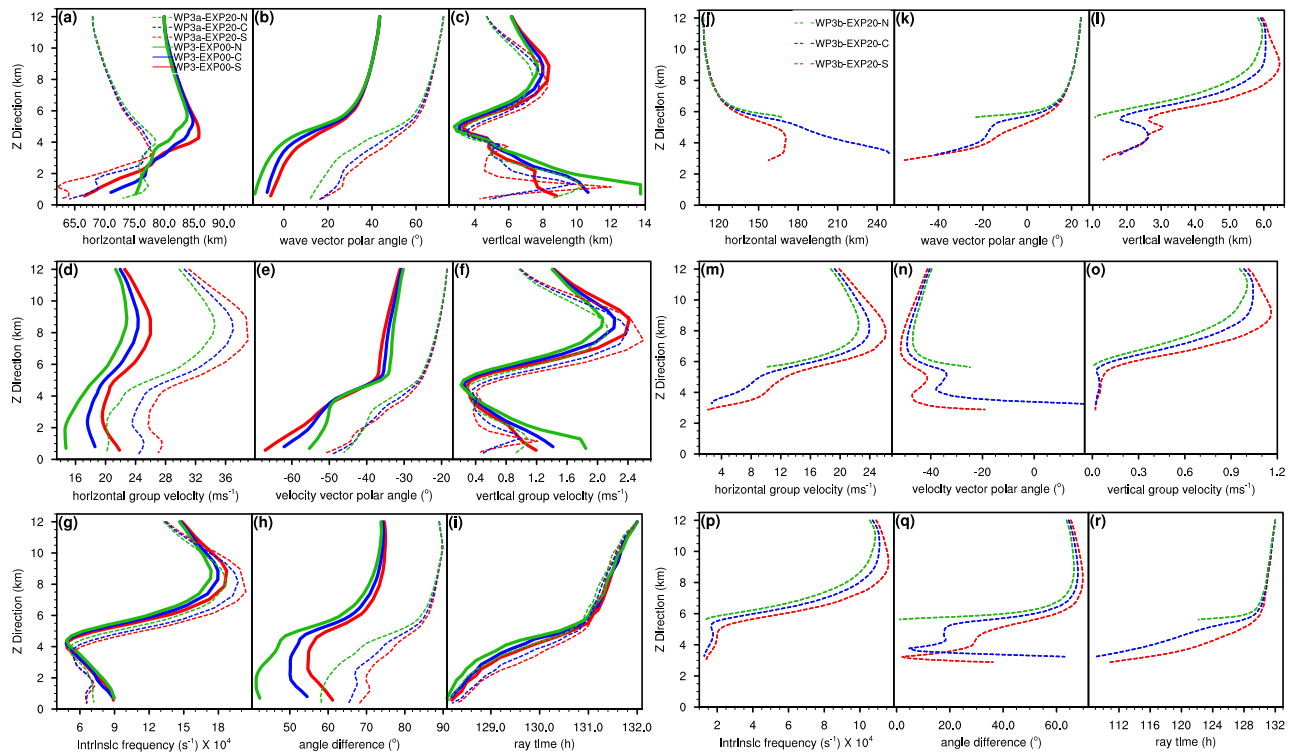


Figure 6. Same as Figure 3, but for selected backtraced rays from (a–i) WP3-EXP00 (solid lines) versus WP3a-EXP20 (dashed lines), and (j–r) WP3b-EXP20 (dash lines) during their backward and downward integrations.

4.5. WP4-EXP00 Versus WP4-EXP20: The Shorter-Scale Wave Packets Above the Cold Front

The examples of the fourth gravity wave mode WP4 in Figures 5c and 5d represent the shorter-scale wave packets located far to the south of the jet right above the tropospheric cold front (its approximate location is marked in Figures 1a and 1b but its wave amplitude at this level/time is too weak to be identified with the contour values of $\pm 2.0 \times 10^{-6} \text{ s}^{-1}$ in horizontal divergence). Similar to WP3 in Figures 5a and 5b, WP4 in either EXP00 (Figure 5c) or EXP20 (Figure 5d) at 132 h is also characterized by its shorter-scale horizontal wavelength λ_H (~ 95 km) with slightly bended structure at 10 km. However, unlike WP3, WP4 has much lower intrinsic frequency Ω (~ 2 to $\sim 3f$ versus ~ 10 to $\sim 15f$), shorter vertical wavelength λ_Z (~ 2 km versus ~ 5 to ~ 6 km), and weaker wave amplitude at 10 km. Note that the wave characteristics between WP4-EXP00 and WP4-EXP20 are almost identical (Table 2).

For the horizontal views of WP4 (Figures 5c and 5d), all the three selected rays can be traced backward directly to the north of their initial points, and they are eventually terminated due to the existence of inertial critical layers at ~ 3 km after an extremely long integration (a potential life span of ~ 50 h; also see Table 2). The ending points of WP4 are located within the tropospheric cold front regions, and they fail to pass through the jet core regions. Subsequent projections of the raypaths onto the horizontal divergence fields show good agreement between the ray tracing analysis and the simulated wave signals during most part of the backtracing (not shown). In addition, the tracing results in WP4-EXP00 are essentially the same as those in WP4-EXP20. Therefore, WP4 is almost certain to initiate from the tropospheric frontal systems, and it is generally not sensitive to the introduction of weak convective instability.

Based on the source mechanism analysis, WP3-EXP00, WP3a-EXP20, WP4-EXP00, and WP4-EXP20 are all very likely to be excited by the tropospheric frontogenesis. However, WP4-EXP00 and WP4-EXP20 are apparently forced by weaker frontal systems at a much earlier time within a region that is away from the jet streams.

4.6. WP5s-EXP00 Versus WP5s-EXP20: The Southern Part of Wave Packets Between Ridge and Trough

Figure 8 shows the examples of the fifth gravity wave mode (WP5; also marked in Figures 1a and 1b) highlighted in WZ14, which refers to the wave packets from the jet exit region in the ridge down to the jet

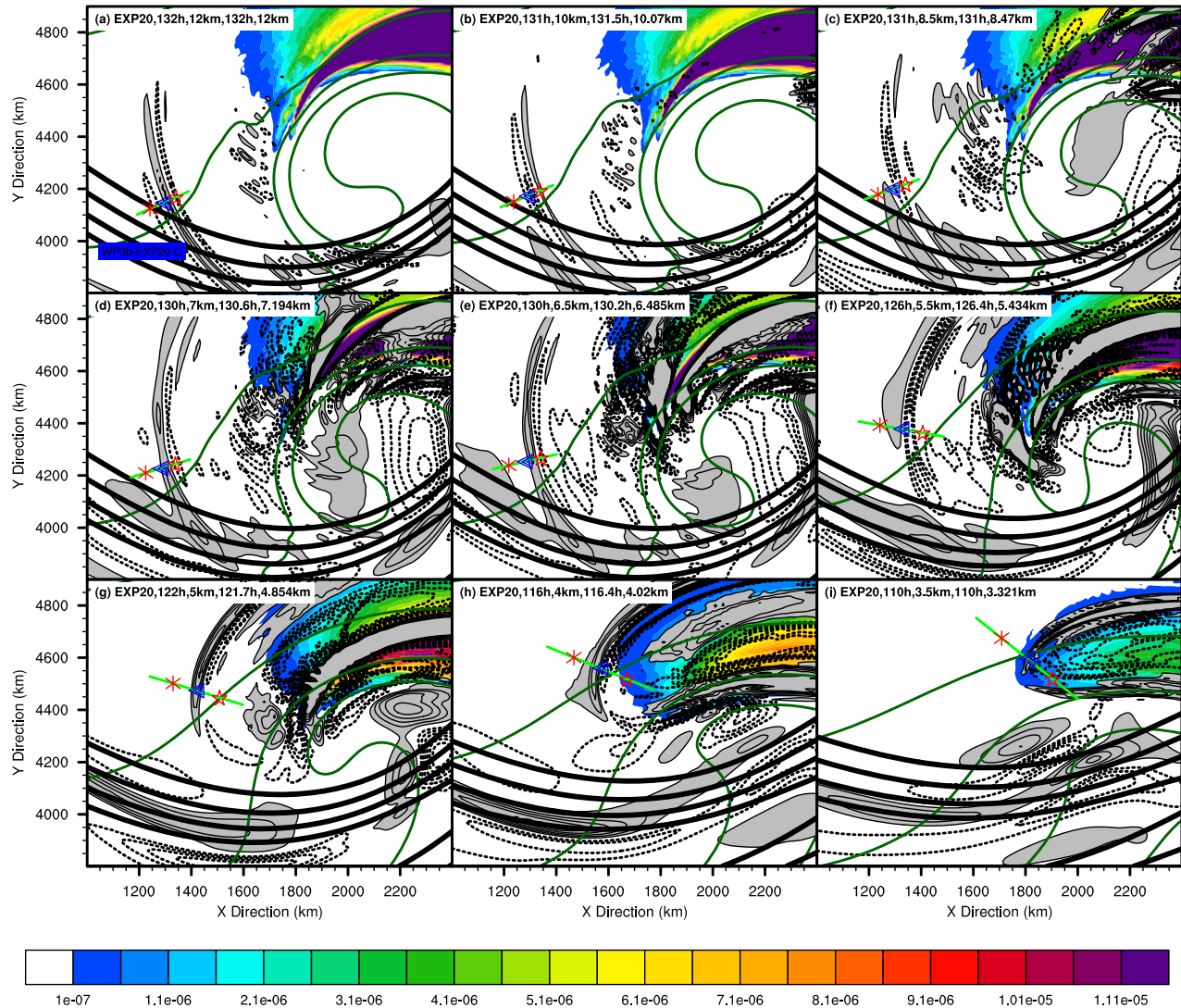


Figure 7. Same as Figure 4, but for WP3b-EXP20-C. The shaded color denotes the vertically averaged positive-only latent heating rate (Ks^{-1}).

entrance region in the trough (also see the cross section study in Figures 8b and 8d of WZ14). WP5s-EXP00 (WP5s-EXP20) represents the southern part of wave packets (WP5s) located just above and almost parallel to the tropopause at 132 h in EXP00 (EXP20), while WP5n-EXP00 (WP5n-EXP20) represents the northern part of wave packets (WP5n) located $\sim 2\text{--}3$ km above the tropopause at 132 h in EXP00 (EXP20). The intrinsic frequencies of WP5s are $1\text{--}2f$, lower than those of WP5n ($3\text{--}4f$). Note that the divergence amplitude related to WP5 in EXP20 is noticeably stronger than that in EXP00. The analysis of WP5n refers to section 4.7.

For the horizontal views of the ray tracing trajectories in WP5s-EXP00 (Figure 8a) and WP5s-EXP20 (Figure 8b), the tracks of the south and center rays can be traced backward to the west in the jet vicinity. Vertically speaking, the south and center rays of WP5s can be eventually traced back to ~ 0.5 to ~ 1.5 km (Table 3). It is suggested in Figures 9a–9i that the propagating wave characteristics and the life cycles of the three selected rays for WP5s are rather different from each other. Note that WP5s-EXP00-N is stopped immediately at the starting position due to its weak initial vertical group velocity (smaller than 0.01 ms^{-1}), and that the integration of WP5s-EXP20-N starts because its initial vertical group velocity is slightly bigger than 0.01 ms^{-1} .

The source analysis for WP5s-EXP00 is indicated in the horizontal views of WP5s-EXP00-C at nine selected levels of EXP00 during its reverse ray tracing (Figure 10). The GROGRAT-simulated position (x, y) and horizontal wave number \vec{K}_H match the WRF-simulated horizontal divergence fields well from 12 to ~ 11 km

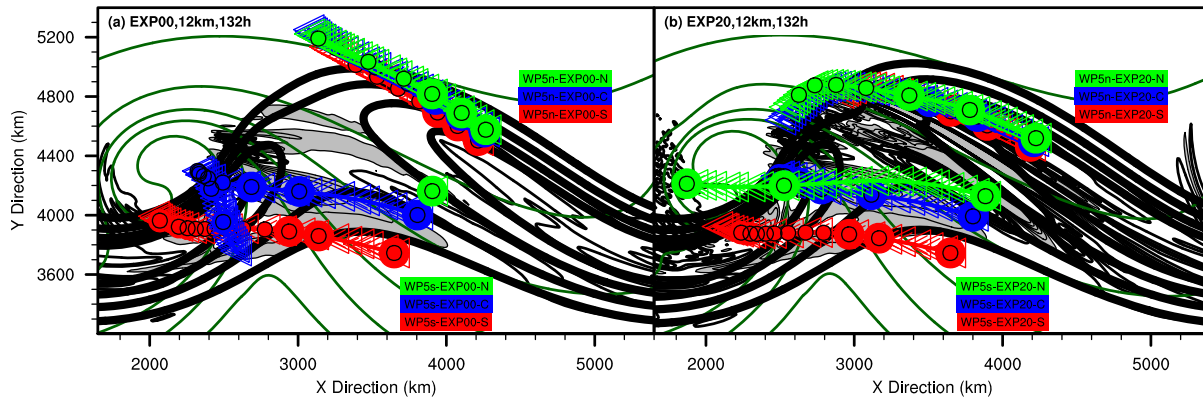


Figure 8. Same as Figure 2, but for (a) WP5s-EXP00 and WP5n-EXP00 in EXP00, and (b) WP5s-EXP20 and WP5n-EXP20 in EXP20. Twelve kilometer horizontal divergence (black contours; positive shaded; $\Delta = 2.0 \times 10^{-6} \text{ s}^{-1}$; range within $\pm 1.2 \times 10^{-5} \text{ s}^{-1}$; zero value omitted) is used in Figure 8a and 8b.

(from 132 to ~ 124 h; Figures 10a–10c). At ~ 120 h (Figure 10d), the ray can be traced back to the immediate jet exit region at ~ 10 km. However, GROGRAT and WRF starts to diverge around ~ 8 to ~ 10 km (~ 118 to ~ 120 h; Figures 10d–10e), since the synoptic-scale horizontal divergence dominates over the potential weak mesoscale wave signals. Below ~ 8 km to the terminated level, the vector of \vec{K}_H slowly rotates in a clockwise direction as the λ_H gradually increases (also see the blue solid line in Figures 9a and 9b). Similarly, WP5s-EXP20-C can also be traced back to the immediate jet exit region within ~ 8 to ~ 10 km with a good agreement between GROGRAT and WRF from 12 km down to 11 km (not shown), even though there is very little rotation of the vector \vec{K}_H for the ray below ~ 8 km (also see the blue dash line in Figure 9b). In one word, it is suggested that the potential source of both WP5s-EXP00 and WP5s-EXP20 may be the upper-level jet (possibly somewhere above ~ 8 to ~ 10 km). Nonetheless, convection may partially impact the amplitude and wave characteristics of WP5s-EXP20, since the upper-level jet exit region is also very close to the low-level convection in the horizontal views.

4.7. WP5n-EXP00 Versus WP5n-EXP20: The Northern Part of Wave Packets Between Ridge and Trough

Due to the small differences in their initial conditions and background information, the horizontal views of the tracks between WP5n-EXP00 (Figure 8a) and WP5n-EXP20 (Figure 8b) are somewhat distinct from one another. For example, the trajectories of WP5n-EXP00 are rather straight (generally along the upper-level jet and 1 km isothermal), while those of WP5n-EXP20 curves at the end of the ray integrations in the left side of the jet exit region (as well as in the region of moist convection). Also, WP5n-EXP00 has a stronger tendency to be traced back to the north than WP5n-EXP20. Vertically speaking, all the rays in both WP5n-EXP00 and WP5n-EXP20 can be traced back to ~ 5 to ~ 7 km (Table 3). The discrepancy between WP5n-EXP00 (three solid lines) and WP5n-EXP20 (three dashed lines) can also be observed in the vertical profile of propagating wave characteristics (Figures 9j–9r). For example, there is a sharp increase in c_{gz} for WP5n-EXP20 between ~ 6 and ~ 7 km, which is not the case for WP5n-EXP00.

The source analysis for WP5n-EXP00 suggests that there is a good agreement between GROGRAT and WRF above the tropopause (not shown), and that WP5n-EXP00-C can be traced back to the tropopause at ~ 6.0 to ~ 6.5 km. Instead, WP5n-EXP20-C can be traced back to the divergence disturbance associated with the initial moist convection below the tropopause. Therefore, the potential source of WP5n-EXP00 may be associated with the disturbance around the tropopause, while the potential source of WP5n-EXP20 may be the initial moist convection or the strengthening frontal systems in the troposphere. Based on the differences in the tracking trajectories, propagating wave characteristics and potential wave energy sources, WP5n-EXP00 and WP5n-EXP20 may be essentially two independent wave packets that propagate into a similar area.

4.8. WP6-EXP20 Versus WP6-EXP100: The Shorter-Scale Wave Packets at the Early Stage of Baroclinic Wave Life Cycle

Figure 11 shows the examples of the sixth gravity wave mode (WP6) in EXP20 and EXP100 that are highlighted in WZ14, which refers to the upper-level shorter-scale wave packets before WP1–WP5 become

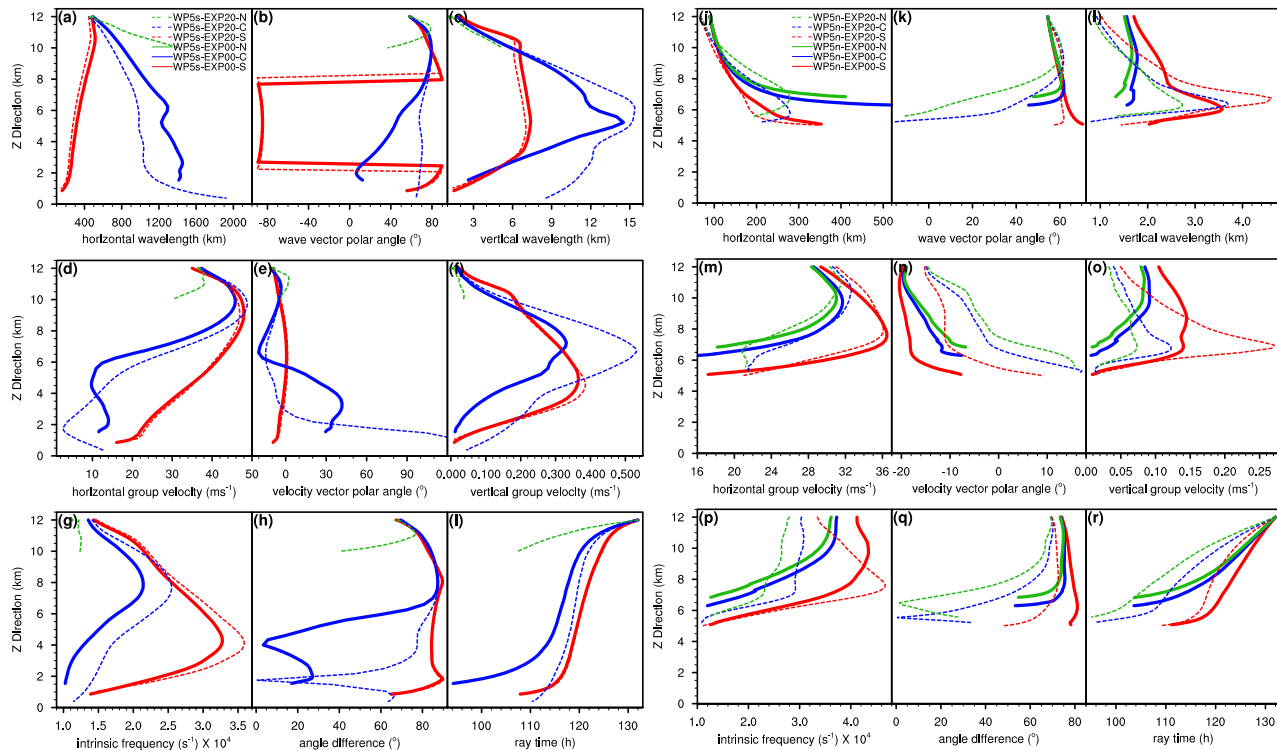


Figure 9. Same as Figure 3, but for selected backtraced rays from (a–i) WP5s-EXP00 (solid lines) versus WP5s-EXP20 (dashed lines), and (j–r) WP5n-EXP00 (solid lines) versus WP5n-EXP20 (dashed lines) during their backward and downward integrations.

mature. While holding the shortest horizontal wavelength among all the gravity wave modes, WP6 has rather high intrinsic frequency with ~ 9 – 12 times the Coriolis parameter. It is also suggested in Figure 11 that the trajectories of WP6 appear to be parallel to the phase lines of WP6 at 12 km. For WP6-EXP20 (WP6-EXP100), all the three selected rays can be traced back to the inertial critical levels at ~ 0.7 km (~ 2.3 km) within only ~ 11 h.

The vertical profiles of the propagating wave characteristics for WP6-EXP20 (three solid lines) and WP6-EXP100 (three dashed lines) are illustrated in Figure 12. Interestingly, it is worth mentioning that the angle δ (equation (1)) between horizontal wave vector (k, l) and ground-based horizontal group velocity vector (c_{gx}, c_{gy}) seems to be close to 90° from 12 km down to ~ 6.5 km within this ~ 2 h integration (Figures 12h–12i). Such a tendency can also be observed in the beginning of the ray integrations for many other wave packets (e.g., WP1 from 12 to ~ 10 km in Figure 3h; WP2 from 12 to ~ 10 km in Figure 3q; WP3a-EXP20 from 12 to ~ 8 km in Figure 6h; WP5n-EXP00 from 12 to ~ 9 km in Figure 9q). Note that the horizontal wave vector (k, l) should always be perpendicular to the intrinsic horizontal group velocity [Holton, 2004], instead of the ground-based horizontal group velocity.

The source analysis of WP6 demonstrates that both WP6-EXP20-C and WP6-EXP100-C pass through the region of latent heating release, and the GROGRAT-simulated rays appears to match the horizontal divergence disturbance quite well through the most part of their life cycles (not shown). Therefore, it is suggested in the ray analysis that the most likely potential mechanism of WP6-EXP20 and WP6-EXP100 should be convection.

5. Propagation Effect Analysis

5.1. Budget Analysis: Background Wind Terms Versus Thermodynamics Terms

To further quantify the impacts of background wind and other physical processes on changing the gravity wave wave numbers, a budget analysis of wave number vector refraction equations is performed. In the right-hand side of the equation (A5d) (A5e; A5f) in Appendix A, which is the wave number vector refraction

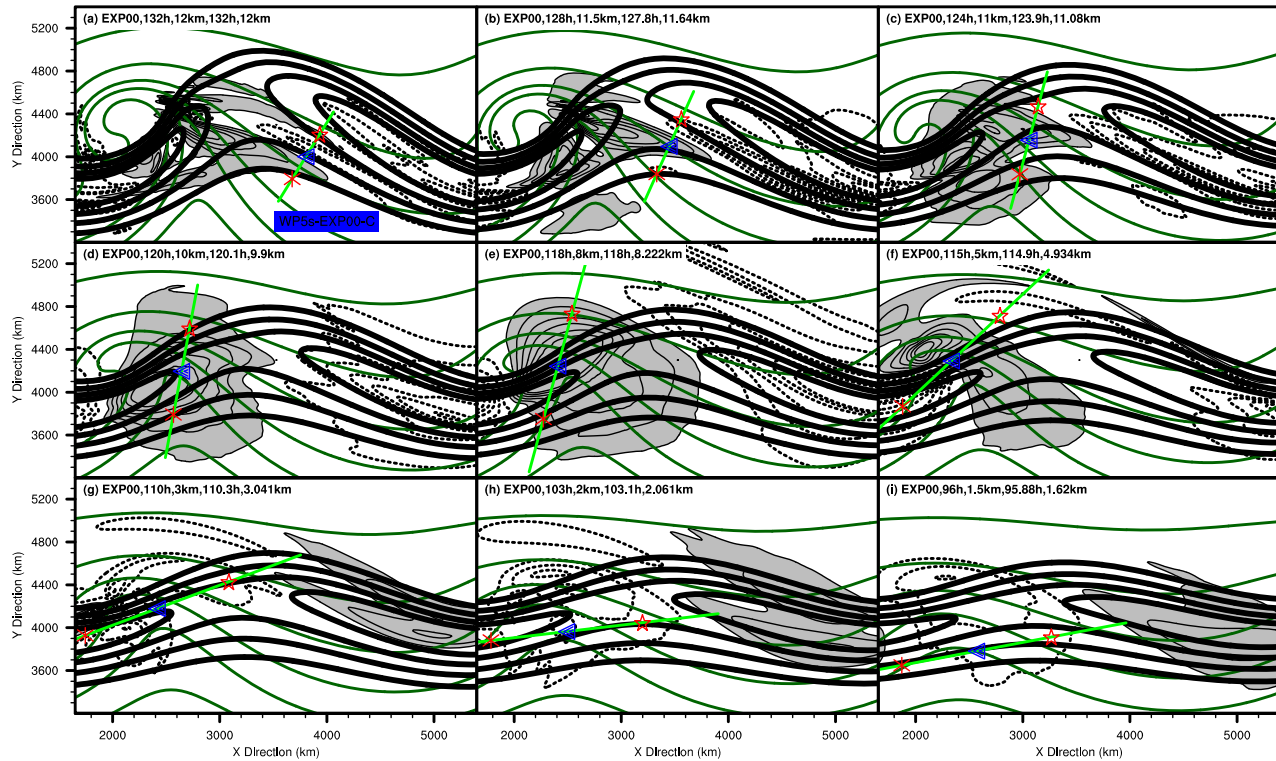


Figure 10. Same as Figure 4, but for WP5s-EXP00-C.

equation in x (y ; z) direction, the sum of the first term and the second term represents the horizontal wind term in x (y ; z) direction, the third term represents the vertical wind term in x (y ; z) direction, the fourth term represents the buoyancy frequency term in x (y ; z) direction, and the fifth term represents the density term in x (y ; z) direction. In addition, the sixth term in equation (A5e) represents the β term in y direction.

The above mentioned terms are compared with each other for all the ray experiments listed in Tables 2 and 3 (not shown). First, the horizontal terms are generally the largest among all for most part of the integrations, regardless of the direction of the equation. Second, the buoyancy frequency terms can be comparable or even larger than the horizontal terms around the tropopause or surface frontal systems, in which there is dramatic change in static stability. Third, the vertical wind terms are almost negligible for most part of the integrations. Fourth, the density terms are negligible for all the tracing experiments. Fifth, the β terms are strictly zero in the current study.

There are two major effects that may refract the wave number vector of gravity waves, including the wind terms and the thermodynamics terms. The wind terms include the horizontal wind terms and the vertical wind terms, and the thermodynamics terms include the buoyancy frequency terms and the density terms. Figure 13 compares the above mentioned two effects for three selected ray tracing experiments (i.e., the center rays of WP1-WP3 in EXP00). Take WP1-EXP00-C as an example, compared with the wind terms (green lines in Figures 13a–13c), the thermodynamics terms (red lines in Figures 13a–13c) are almost negligible from 12 km down to ~ 8 km, as well as below ~ 4.5 km. For the region between ~ 8 and ~ 4.5 km, the thermodynamics terms apparently enhance the effect of the wind terms in the x direction, but they instead largely cancel the effect of the wind terms in the y and z direction (also see the sum of both effects in the black lines of Figures 13a–13c). Since the vertical wave number is negative for an upward propagating wave packet, it is expected that any negative (positive) term in the z direction of the wave number vector refraction equations (i.e., the right-hand side of equation (A5f)) will further increase (decrease) the absolute value of the vertical wave number and shorten (elongate) the vertical wavelength. Therefore, the thermodynamics terms tend to shorten the vertical wavelength for the region between ~ 8 and ~ 4.5 km, while the wind terms tend to elongate (shorten) the vertical wavelength for the region below ~ 4.5 (above ~ 8 km). Similar discussions on the comparison between the wind terms and the thermodynamics terms can also be

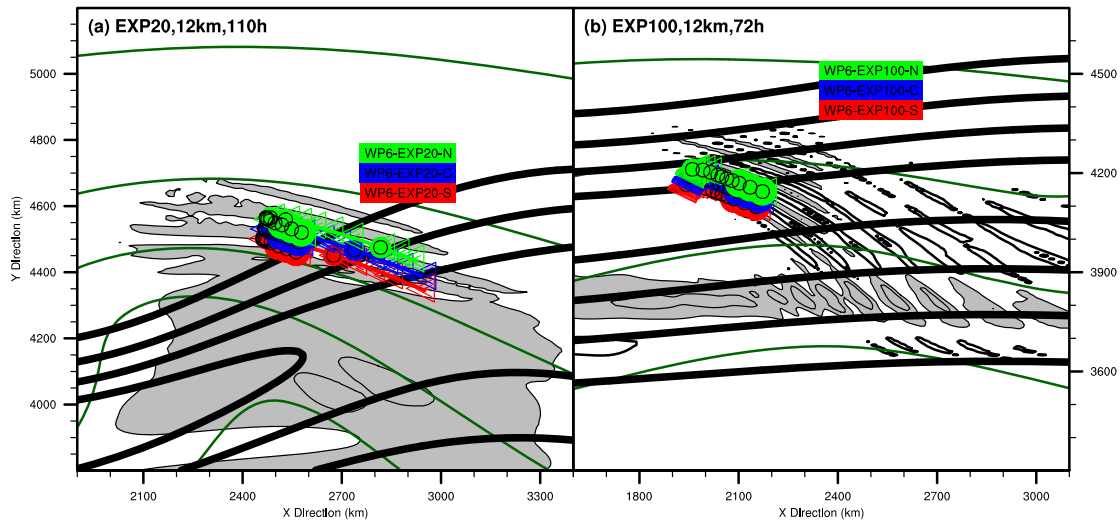


Figure 11. Same as Figure 2, but for (a) WP6-EXP20 in EXP20, and (b) WP6-EXP100 in EXP100. Twelve kilometer horizontal divergence (black contours; positive shaded; $\Delta = 2.0 \times 10^{-6} \text{ s}^{-1}$; range within $\pm 1.2 \times 10^{-5} \text{ s}^{-1}$; zero value omitted) is used in Figures 11a and 11b.

addressed in the examples of WP2-EXP00-C (Figures 13d–13f) and WP3-EXP00-C (Figures 13g–13i). In addition, the budget analysis also suggests that the thermodynamics terms in z direction are negative generally for all the rays crossing the tropopause (not shown), even though their amplitudes and height levels vary widely from case to case.

5.2. Forward Ray Tracing of WP5s-EXP00: Full GROGRAT Versus Modified GROGRAT

In order to understand the propagating effect for the baroclinic jet exit gravity waves, five selected forward ray experiments are performed for the case of WP5s-EXP00. The initial parameters in the center ray WP5s-EXP00-C-F use the same parameters in the reverse ray tracing integrations of WP5s-EXP00-C at ~ 120 h and ~ 10 km (also see Figure 10d), but the tracing model is integrated forward in time and upward in altitude. Another four rays (south ray, named as WP5s-EXP00-S-F; the ray between center ray and south ray, named as WP5s-EXP00-CS-F; the ray between center ray and north ray, named as WP5s-EXP00-CN-F; north ray, named as WP5s-EXP00-N-F) are launched along the horizontal wave number vector with the same direct input parameters of wave characteristics as those in the center ray. Figure 14a demonstrates that all the above mentioned five rays propagate downstream to the east of their initial positions in the horizontal views. Also, the vertical penetrations of the rays between 11 and 12 km are apparently weaker than those between 10 and 11 km. In addition, WP5s-EXP00-CN-F and WP5s-EXP00-N-F have slower vertical propagations than the other rays.

The wind effect and the thermodynamics effect for the five selected rays are further compared in Figure 15. As to the wind effect (Figures 15a–15c for the x-z directions), except for the WP5s-EXP00-CS-F and WP5s-EXP00-S-F in y direction, all the wind terms generally share negative values. In particular, for the wind terms in x or y direction, WP5s-EXP00-CN-F and WP5s-EXP00-N-F generally have the smallest negative values. Instead, the smallest negative values of the wind terms in z direction are found in WP5s-EXP00-C-F. As to the thermodynamics effect (Figures 15d–15f for the x-z directions), it is interesting to point out that there are noticeable negative thermodynamics terms for WP5s-EXP00-CS-F and WP5s-EXP00-S-F in y or z direction, even though the thermodynamics terms are almost negligible in other ray experiments. Note that the negative values between the wind terms and the thermodynamics terms are generally comparable in z direction for WP5s-EXP00-CS-F and WP5s-EXP00-S-F.

In order to understand the importance of thermodynamics effect and its sensitivity to ray trajectories and propagating characteristics, GROGRAT codes are modified to eliminate the thermodynamics terms in equations (A5d)–(A5f). Another five forward ray experiments are performed for the case of WP5s-EXP00 but with modified GROGRAT (see Figure 14b for their ray trajectories in horizontal views). It is shown in Figures 14a and 14b that there is almost no difference between modified GROGRAT and full GROGRAT in the ray trajectories for WP5s-EXP00-N-F, WP5s-EXP00-CN-F, and WP5s-EXP00-C-F. However, WP5s-EXP00-CS-F and WP5s-

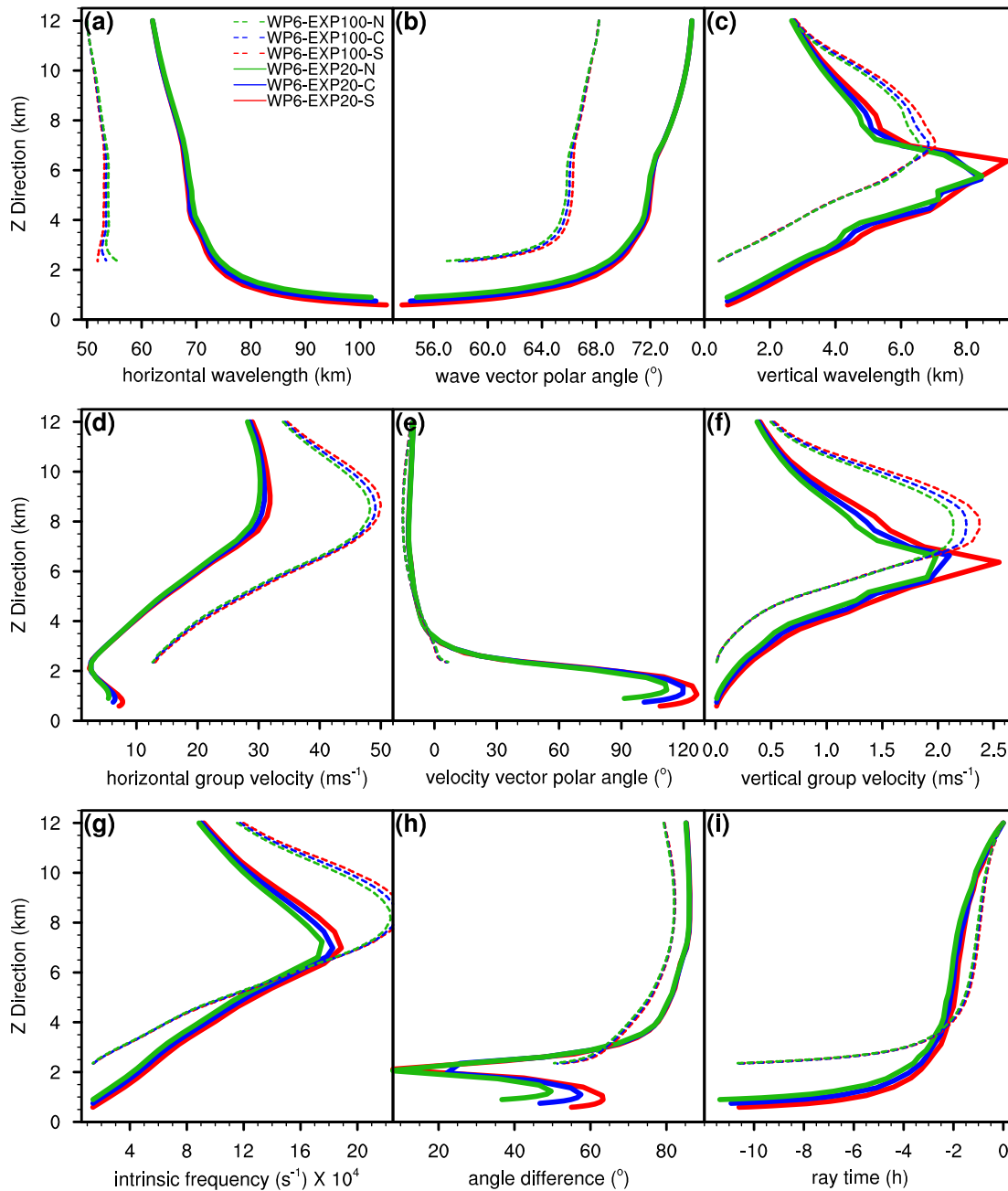


Figure 12. Same as Figure 3, but for selected backtraced rays from (a-i) WP6-EXP20 (solid lines) versus WP6-EXP100 (dash lines) during their backward and downward integrations. Unlike Figure 3i, the ray time in Figure 12i shows the difference between the original ray time and its corresponding initial ray time, in order to eliminate the initial ray time differences between WP6-EXP20 and WP6-EXP100.

EXP00-S-F in modified GROGRAT (red lines in Figure 14b) apparently have stronger tendencies to travel toward the south than those in full GROGRAT (red lines in Figure 14a).

Figure 16 compares the vertical profiles of the propagating wave characteristics between the above mentioned ray experiments with full GROGRAT (control experiments; Figures 16a–16i) and those with modified GROGRAT (sensitivity experiments; Figures 16j–16r). During the propagations in control experiments (Figures 16a–16i), both horizontal wavelengths λ_H and vertical wavelength λ_Z decrease in all the rays from ~ 10 to ~ 12 km, except for λ_H in WP5s-EXP00-S-F. The decreasing vertical group velocities c_{gz} in all the rays suggest the presence of potential critical levels. The intrinsic frequencies Ω are around the inertial limit of gravity waves, a suggested value of $\sqrt{2}f$ [also see Wang *et al.*, 2009, 2010]. The shrinkages of wavelengths in all experiments (except for the south ray) appear to be consistent with the wave capture mechanism for

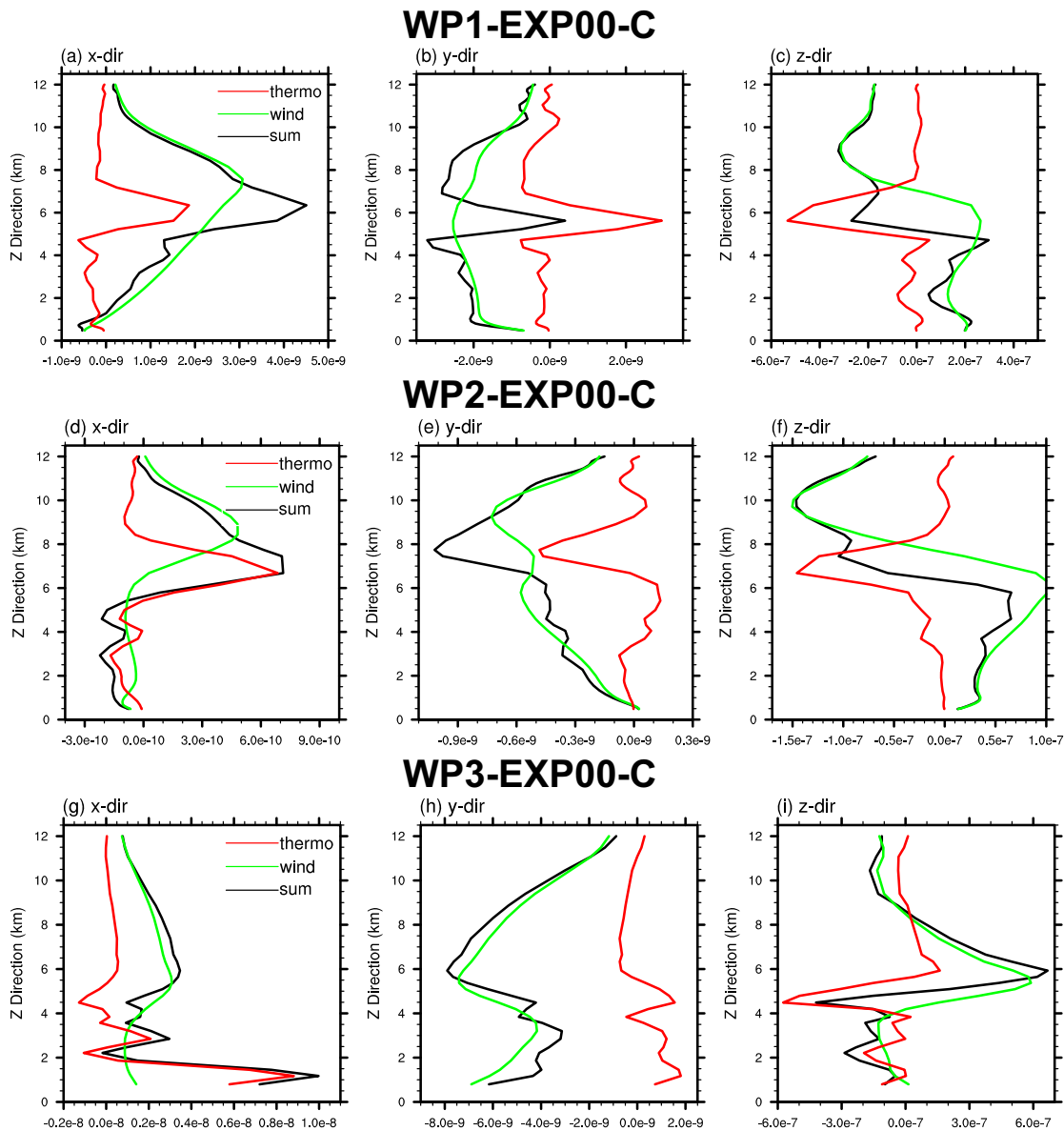


Figure 13. The vertical profiles of the budget analysis ($m^{-1}s^{-1}$) for (a–c) WP1-EXP00-C, (d–f) WP2-EXP00-C, and (g–i) WP3-EXP00-C. The left (middle; right) column represents the budget analysis in the right-hand side of equation (A5d) (equation (A5e); equation (A5f)), which is the wave number vector refraction equation in x (y; z) direction. The red (green; black) lines represent the thermodynamics terms (the wind terms; the sum of both thermodynamics terms and wind terms).

gravity waves in a specific wind structure that has constant horizontal deformation and constant vertical wind shear [Badulin and Shrira, 1993; Bühler and McIntyre, 2005; Plougonven and Snyder, 2005]. Similar behaviors can also be found in ray tracing analysis for the idealized midlevel vortex dipole [e.g., Wang et al., 2009, Figure 8]. However, the sensitivity experiments in Figures 16j–16r suggest that the decrease of λ_H and λ_Z are dramatically weakened or even removed for WP5s-EXP00-CS-F and WP5s-EXP00-S-F. These results suggest that background effects (including horizontal deformation and vertical shear) may not be very efficient for the potential process of wave capturing in WP5s-EXP00-CS-F and WP5s-EXP00-S-F. In other words, the tendencies of shrinkages in wavelengths (a seemingly behavior for capturing waves caused by wind effects only) may be partially/largely forced by thermodynamics effects for the baroclinic jet exit gravity waves in some particular cases.

6. Concluding Remarks and Discussion

Using a four-dimensional ray-tracing technique, this study investigates the propagating wave characteristics, potential source mechanisms, and wave number vector refraction budget of six groups of lower-

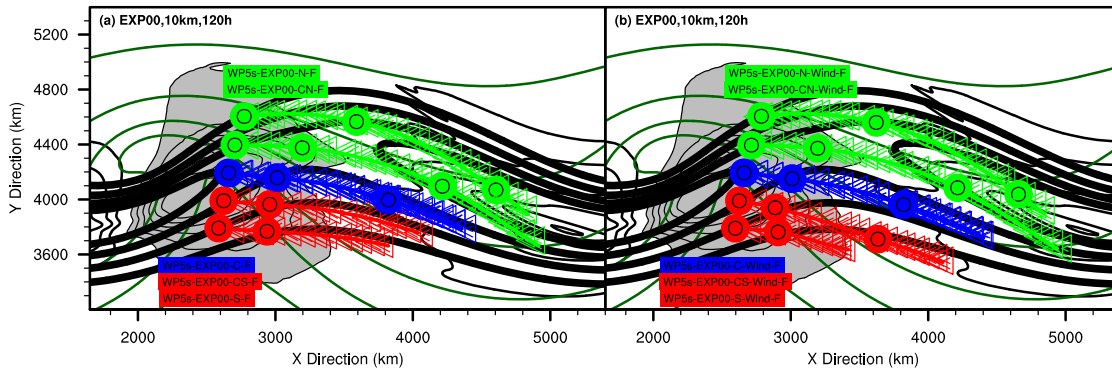


Figure 14. Same as Figure 2, but for the horizontal views of five selected forward ray tracing paths for (a) WP5s-EXP00 that start from ~10 km at 120 h, and (b) their corresponding sensitivity experiments with modified ray tracing equations which eliminate all the thermodynamics terms in the wave number vector refraction equation (equations (A5d)–(A5f)).

stratospheric gravity waves simulated in the idealized moist baroclinic jet-front system of WZ14. The 3 h saved 30 km WRF output is ingested into the ray-tracing model to account for the four-dimensional background variations. The location and wave characteristics of each wave packet, estimated with a two-dimensional Fourier decomposition and verified with linear theory in WZ14, are selected as the endpoint of each raypath from which the ray-tracing model is integrated backward in time and downward in altitude.

On one hand, the resemblances between EXP00 and EXP20 in ray-tracing analysis demonstrate the limitation of moisture in modifying certain dry waves. Consistent with the past source mechanism study of LZ08 on tracking gravity waves in the dry idealized baroclinic jet-front systems of Z04, the current study continues to suggest that the short-scale WP1-EXP00 in the jet-exit region may originate from the upper-tropospheric jet-front system and/or the surface frontal system, while the medium-scale WP2-EXP00 originate from the upper-tropospheric jet imbalance. It is again confirmed that both WP3-EXP00 in the deep

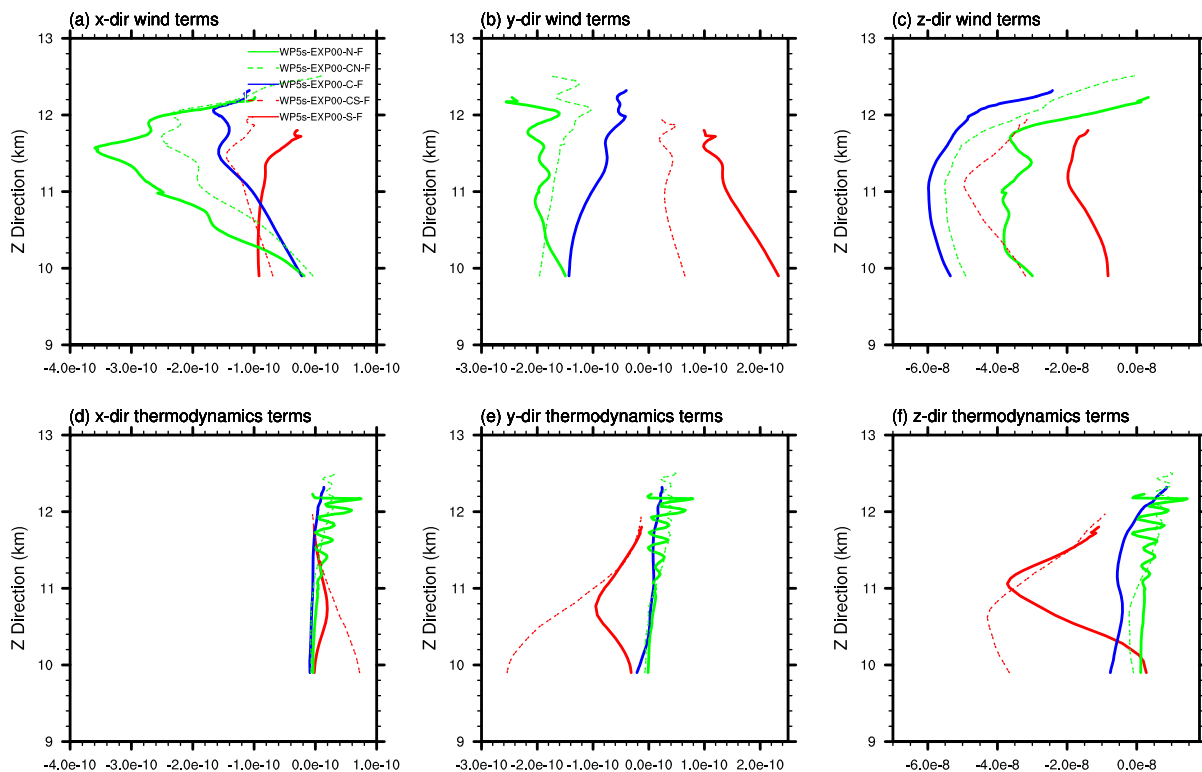


Figure 15. The vertical profiles of the budget analysis ($m^{-1}s^{-1}$) for the five selected forward ray tracing paths in WP5s-EXP00. Five different lines represent the above five experiments. The left (middle; right) column represents the budget analysis in the right-hand side of equation (A5d) (equation (A5e); equation (A5f)), which is the wave number vector refraction equation in x (y; z) direction. The top (bottom) plots represent the wind terms (the thermodynamics terms).

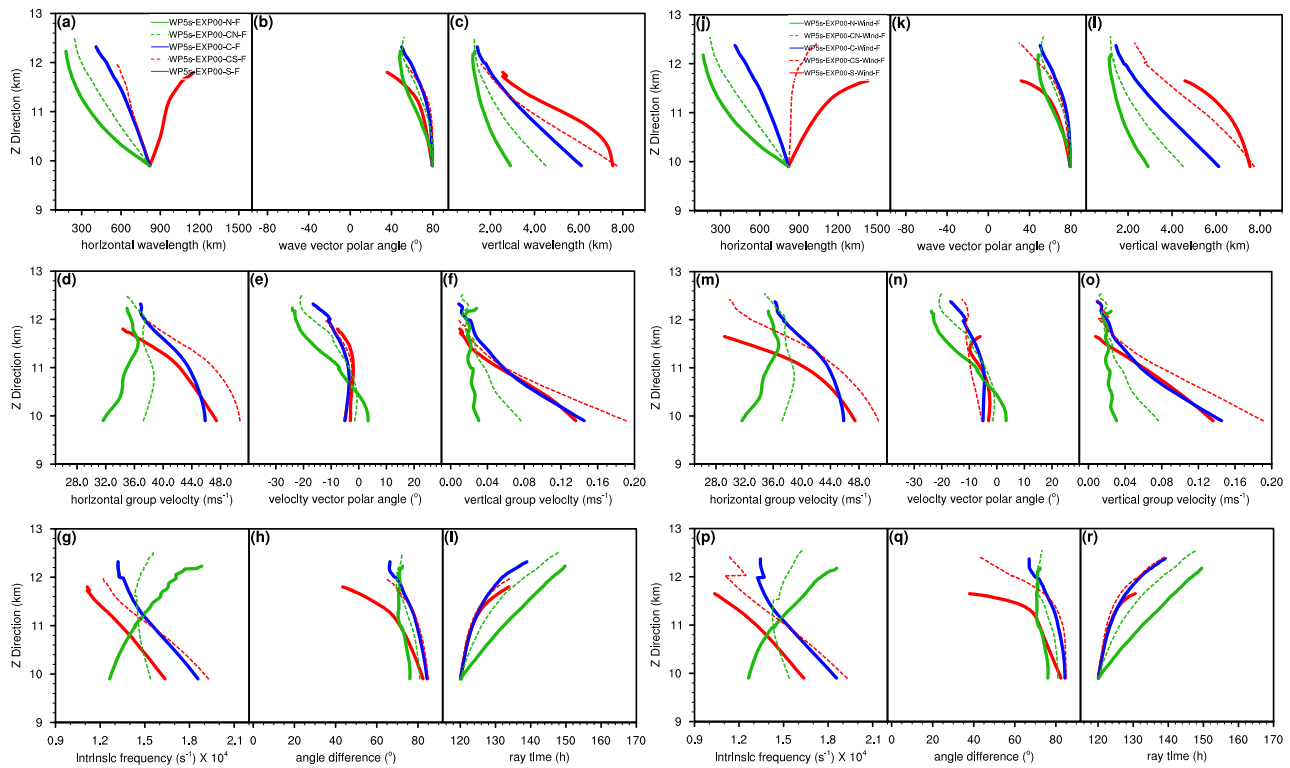


Figure 16. Same as Figure 3, but for five selected forward ray tracings from (a–i) WP5s-EXP00 that start from ~ 10 km at ~ 120 h, and (j–r) their corresponding sensitivity experiments with modified ray tracing equations which eliminate all the thermodynamics terms in the wave number vector refraction equation (equations (A5d)–(A5f)).

trough region across the jet and WP4-EXP00 right above the cold fronts are almost certain to initiate from the frontal system. Interestingly, WP1, WP2, and WP4 share rather similar trajectories and wave characteristics along the raypaths between EXP00 and EXP20 (listed in Table 2), most likely due to the similarity in observed wave characteristics and evolving background variations. This implies that those three above mentioned wave packets in both EXP00 and EXP20 are controlled by dry dynamical processes, and that moist processes have little impact on their generation and propagation.

On the other hand, based on the differences in ray-tracing analysis between EXP00 and EXP20 (examples are summarized in Table 3), moist convection may impact gravity wave fields in several aspects. First, moist convection could be considered as a new wave energy source (e.g., WP6-EXP20 or WP6-EXP100 observed directly above the heating). Second, moist convection may partially/locally modify the dry source or background flow (e.g., see the discussion in section 4.3 on the ray tracing comparison between WP3-EXP00 and WP3a-EXP20). Third, convectively generated gravity waves or convectively enhanced frontogenesis gravity waves could slowly propagate upstream of the latent heating (e.g., WP3b-EXP20 can be slowly traced back to the leading edge of amplifying convection associated with the developing front) and downstream of the latent heating (e.g., section 4.7 highlights the discrepancy in the trajectories and changing wave characteristics between WP5n-EXP00 and WP5n-EXP20).

A budget analysis of wave number vector refraction equations is performed for the six groups of gravity waves to further quantify the impacts of wind effect and thermodynamics effect on changing the gravity wave wave numbers. It is found in the current study that the horizontal wind terms are the main contributor to wind effect and that the vertical wind terms are secondary in most cases. The thermodynamics effect is fully controlled by the buoyancy frequency terms, while the density terms are almost negligible. Generally speaking, the wind effect dominates over the thermodynamics effect, and the spatial and temporal variability of the complex background wind appears to have a very strong influence on the characteristics of propagating gravity waves. However, the thermodynamics effect may counteract, enhance, or even take over the effect of background wind for those wave packets crossing the tropopause or frontal systems. Based on the forward ray experiments of WP5s-EXP00, there may be sensitivity to the inclusion/exclusion of the

thermodynamics effect for certain baroclinic jet exit wave packets in their ray trajectories (e.g., the tendency of southward propagation) and the propagating wave characteristics (e.g., the shrinkage in wavelengths).

It is argued again in this article that gravity wave emissions can be excited by the evolving baroclinic jet under spontaneous balance adjustment hypothesis [Plougonven and Zhang, 2007], and that the propagations of the excited gravity waves are continuous in the changing background flow. For example, the ray tracing analysis suggests that WP2-EXP00 and WP5s-EXP00 may be both generated by upper-level jet, but there are two major discrepancies between these two wave packets. First, the timings of the wave generations may be different. WP2-EXP00 may be excited at ~ 129 h while WP5s-EXP00 may be generated at ~ 120 h. Accordingly, the orientation, shape, and strength of the baroclinic jet are expected to be different when these two wave packets are generated. Second, the background information for the wave propagation may be also different. In other words, the discrepancies between WP2-EXP00 and WP5s-EXP00 may be attributed to the continuous change in their source and associated background flow over a long time. Similar to the waves forced by jet, the generation and propagation of gravity waves induced by either frontogenesis (e.g., WP3-EXP00) or convection (e.g., WP6-EXP100) may be also considered as a continuous process. Note that both the source and background flow are quasi-stationary in the vortex-dipole jet case [Wang et al., 2009] relative to the baroclinic jet-front case in WZ14.

Appendix A: Ray Tracing Equation

The ray tracing equation, which describes the propagating trajectory and wavenumber vector refraction, can be given as below [see Plougonven and Zhang, 2014, section 4.2]:

$$\frac{d_g \vec{X}}{dt} = \frac{\partial \omega}{\partial \vec{K}}, \quad (\text{A1})$$

$$\frac{d_g \vec{K}}{dt} = -\frac{\partial \omega}{\partial \vec{X}}, \quad (\text{A2})$$

where vector \vec{X} is the location of wave packet (x , y , and z for three components), vector \vec{K} is wave number vector (k , l , and m in x , y , and z direction), t is time, and ω is the absolute frequency or the ground-based frequency. Here $\frac{d_g}{dt} = \frac{\partial}{\partial t} + \vec{c}_g \cdot \nabla$, in which \vec{c}_g is ground-based group velocity (c_{gx} , c_{gy} , and c_{gz} in x , y , and z direction) and \vec{c}_g is equal to the right-hand side of equation (A1) (i.e., $\vec{c}_g = \frac{\partial \omega}{\partial \vec{K}}$). In addition, the absolute frequency ω can also be expressed as follows.

$$\omega = \Omega + \vec{U} \cdot \vec{K}, \quad (\text{A3})$$

where vector \vec{U} is the background wind (u , v , and w in x , y , and z direction), and Ω is the intrinsic frequency or the frequency in the frame moving with the fluid. The intrinsic frequency of the gravity waves Ω can be derived as below based on the dispersion for plane waves [e.g., Fritts and Alexander, 2003, equation (23)].

$$\Omega^2 = \frac{N^2(k^2 + l^2) + f^2(m^2 + \alpha^2)}{k^2 + l^2 + m^2 + \alpha^2}, \quad (\text{A4})$$

where f is the Coriolis parameter; N is the buoyancy frequency; $\alpha = \frac{1}{2H_\rho}$, where H_ρ is the density scale height ($H_\rho = \left(-\frac{\partial \rho_0 / \partial z}{\rho_0}\right)^{-1}$, where ρ_0 is density).

Based on equations (A1)–(A4), the complete ray tracing equation can also be expanded as follows [Marks and Eckermann, 1995]

$$\frac{d_g x}{dt} = u + \frac{k(N^2 - \Omega^2)}{\Omega \Delta}, \quad (\text{A5a})$$

$$\frac{d_g y}{dt} = v + \frac{l(N^2 - \Omega^2)}{\Omega \Delta}, \quad (\text{A5b})$$

$$\frac{d_g z}{dt} = w - \frac{m(\Omega^2 - f^2)}{\Omega \Delta}, \quad (\text{A5c})$$

$$\frac{d_g k}{dt} = -ku_x - lv_x - mw_x - \frac{N_x^2(k^2 + l^2)}{2\Omega\Delta} + \frac{\alpha_x^2(\Omega^2 - f^2)}{2\Omega\Delta}, \quad (\text{A5d})$$

$$\frac{d_g l}{dt} = -ku_y - lv_y - mw_y - \frac{N_y^2(k^2 + l^2)}{2\Omega\Delta} + \frac{\alpha_y^2(\Omega^2 - f^2)}{2\Omega\Delta} - \frac{ff_y(m^2 + \alpha^2)}{\Omega\Delta}, \quad (\text{A5e})$$

$$\frac{d_g m}{dt} = -ku_z - lv_z - mw_z - \frac{N_z^2(k^2 + l^2)}{2\Omega\Delta} + \frac{\alpha_z^2(\Omega^2 - f^2)}{2\Omega\Delta}, \quad (\text{A5f})$$

where $\Delta = k^2 + l^2 + m^2 + \alpha^2$; subscripts of x , y , and z represent partial derivatives over x , y , and z ; $N_x^2 = (N^2)_x$, and so on. Equations (A5a)–(A5c) indicates that the local speed at any point along the ray is determined by ground-based group velocity \vec{c}_g instead of background wind \vec{U} . Equations (A5d)–(A5f) suggests that the refraction of wave number vector can be attributed to the partial spatial derivatives of background wind (i.e., u , v , and w), the partial spatial derivatives of the square of buoyancy frequency (i.e., N^2), the partial spatial derivatives of α^2 , and β effect (i.e., f_y).

Acknowledgments

We are very grateful to Shuguang Wang for helping setting up the ray tracing experiments. This research is supported by the National Science Foundation under grants 0904635 and 1114849. Computing is performed at the Texas Advanced Computing Center (TACC). All data are freely available from sources indicated in the text or from the corresponding author upon request (Email: jwei@psu.edu).

References

- Alexander, M. J., J. R. Holton, and D. R. Durran (1995), The gravity wave response above deep convection in a squall line simulation, *J. Atmos. Sci.*, *52*, 2212–2226.
- Aspden, J., and J. Vanneste (2010), Inertia-gravity-wave generation: A geometric-optic approach, in *IUTAM Symposium on Turbulence in the Atmosphere and Oceans*, edited by D. Dritschel, pp. 17–26, Springer, Netherlands.
- Badulin, S. I., and V. I. Shrira (1993), On the irreversibility of internal waves dynamics due to wave-trapping by mean flow inhomogeneities. Part 1. Local analysis, *J. Fluid Mech.*, *251*, 21–53.
- Blumen, W. (1972), Geostrophic adjustment, *Rev. Geophys. Space Phys.*, *10*, 485–528.
- Bosart, L. F., W. E. Bracken, and A. Seimon (1998), A study of cyclone mesoscale structure with emphasis on a large-amplitude inertia-gravity waves, *Mon. Weather Rev.*, *126*, 1497–1527.
- Broutman, D. (1984), The focusing of short internal waves by an inertial wave, *Geophys. Astrophys. Fluid Dyn.*, *30*, 199–225, doi:10.1080/03091928408222850.
- Bühler, O. (2009), *Waves and Mean Flows*, p. 341, Cambridge Univ. Press, Cambridge, U. K.
- Bühler, O., and M. E. McIntyre (2005), Wave capture and wave-vortex duality, *J. Fluid Mech.*, *534*, 67–95.
- Cahn, A. (1945), An investigation of the free oscillations of a simple current system, *J. Meteorol.*, *2*, 113–119.
- Clark, T. L., T. Hauf, and J. P. Kuettnner (1986), Convectively forced internal gravity waves: Results from two-dimensional numerical experiments, *Q. J. R. Meteorol. Soc.*, *112*, 899–925.
- Dunkerton, T. J., and N. Butchart (1984), Propagation and selective transmission of internal gravity waves in a sudden warming, *J. Atmos. Sci.*, *41*, 1443–1460.
- Eckermann, S., and C. Marks (1996), An idealized ray model of gravity wave tidal interactions, *J. Geophys. Res.*, *101*, 21,195–21,212.
- Eckermann, S., and C. Marks (1997), GROGRAT: A new model of the global propagation and dissipation of atmospheric gravity waves, *Adv. Space Res.*, *20*(6), 1253–1256.
- Fovell, R., D. Durran, and J. R. Holton (1992), Numerical simulations of convectively generated stratospheric gravity waves, *J. Atmos. Sci.*, *49*, 1427–1442.
- Fritts, D. C., and M. J. Alexander (2003), Gravity wave dynamics and effects in the middle atmosphere, *Rev. Geophys.*, *41*(1), 1003, doi:10.1029/2001RG000106.
- Gerrard, A. J., T. J. Kane, S. D. Eckermann, and J. P. Thayer (2004), Gravity waves and mesospheric clouds in the summer middle atmosphere: A comparison of lidar measurements and ray modeling of gravity waves over Sondrestrom, Greenland, *J. Geophys. Res.*, *109*, D10103, doi:10.1029/2002JD002783.
- Griffiths, M., and M. J. Reeder (1996), Stratospheric inertia-gravity waves generated in a numerical model of frontogenesis. I: Model solutions, *Q. J. R. Meteorol. Soc.*, *122*, 1153–1174.
- Guest, F., M. Reeder, C. Marks, and D. Karoly (2000), Inertia gravity waves observed in the lower stratosphere over Macquarie Island, *J. Atmos. Sci.*, *57*, 737–752.
- Gutowski, W. J., L. E. Branscome, and D. A. Stewart (1992), Life cycles of moist baroclinic eddies, *J. Atmos. Sci.*, *49*, 306–319, doi:10.1175/1520-0469(1992)049<0306:LCOMBE>2.0.CO;2.
- Hertzog, A., C. Souprayen, and A. Hauchecorne (2001), Observation and backward trajectory of an inertia-gravity wave in the lower stratosphere, *Ann. Geophys.*, *19*, 1141–1155.
- Holton, J. R. (2004), *An Introduction to Dynamic Meteorology*, 4th ed., 535 pp., Elsevier, N. Y.
- Hooke, W. H. (1986), Gravity waves, in: *Mesoscale Meteorology and Forecasting*, edited by P. S. Ray, pp. 272–288, *Amer. Meteorol. Soc.* [Available at <http://bookstore.ametsoc.org/catalog/book/mesoscale-meteorology-and-forecasting>.]
- Jewett, B. F., M. K. Ramamurthy, and R. M. Rauber (2003), Origin, evolution, and finescale structure of the St. Valentine's day mesoscale gravity wave observed during storm-fest. Part iii: Gravity wave genesis and the role of evaporation, *Mon. Weather Rev.*, *131*, 617–633.
- Jones, W. L. (1969), Ray tracing for internal gravity waves, *J. Geophys. Res.*, *74*, 2028–2033.
- Kim, Y.-J., S. D. Eckermann, and H.-Y. Chun (2003), An overview of the past, present and future of gravity-wave drag parametrization for numerical climate and weather prediction models, *Atmos. Ocean*, *41*, 65–98.
- Klemp, J. B., J. Dudhia, and A. D. Hassiotis (2008), An upper gravity-wave absorbing layer for NWP applications, *Mon. Weather Rev.*, *136*, 3987–4004.
- Koch, S. E., and P. B. Dorian (1988), A mesoscale gravity wave event observed during CCOPE. Part III: Wave environment and probable source mechanisms, *Mon. Weather Rev.*, *116*, 2570–2592.
- Koch, S. E., F. Zhang, M. Kaplan, Y.-L. Lin, R. Weglarz, and M. Trexler (2001), Numerical simulation of a gravity wave event observed during CCOPE. Part 3: The role of a mountain-plains solenoid in the generation of the second wave episode, *Mon. Weather Rev.*, *129*, 909–932.

- Lane, T. P., and M. J. Reeder (2001), Convectively generated gravity waves and their effect on the cloud environment, *J. Atmos. Sci.*, *58*, 2427–2440.
- Lighthill, J. M. (1978), *Waves in Fluids*, Cambridge Univ. Press, Cambridge, U. K.
- Lin, Y., and F. Zhang (2008), Tracking gravity waves in baroclinic jet-front systems, *J. Atmos. Sci.*, *65*, 2402–2415.
- Lin, Y.-L., R. D. Farley, and H. D. Orville (1983), Bulk parameterization of the snow field in a cloud model, *J. Clim. Appl. Meteorol.*, *22*, 1065–1092.
- Marks, C. J., and S. D. Eckermann (1995), A three-dimensional nonhydrostatic ray-tracing model for gravity waves: Formulation and preliminary results for the middle atmosphere, *J. Atmos. Sci.*, *52*, 1959–1984.
- Mirzaei, M., C. Zülicke, A. Mohebalhojeh, F. Ahmadi-Givi, and R. Plougonven (2014), Structure, energy, and parameterization of inertia-gravity waves in dry and moist simulations of a baroclinic wave life cycle, *J. Atmos. Sci.*, *71*, 2390–2414. doi:10.1175/JAS-D-13-075.1. [Available at <http://journals.ametsoc.org/doi/abs/10.1175/JAS-D-13-075.1>]
- O'Sullivan, D., and T. J. Dunkerton (1995), Generation of inertia-gravity waves in a simulated life cycle of baroclinic instability, *J. Atmos. Sci.*, *52*, 3695–3716.
- Plougonven, R., and C. Snyder (2005), Gravity waves excited by jets: Propagation versus generation, *Geophys. Res. Lett.*, *32*, L18892, doi:10.1029/2005GL023730.
- Plougonven, R., and C. Snyder (2007), Inertia-gravity waves spontaneously generated by jets and fronts. Part I: Different baroclinic life cycles, *J. Atmos. Sci.*, *64*, 2502–2520.
- Plougonven, R., and F. Zhang (2007), On the forcing of inertia-gravity waves by synoptic-scale flows, *J. Atmos. Sci.*, *64*, 1737–1742.
- Plougonven, R., and F. Zhang (2014), Internal gravity waves from atmospheric jets and fronts, *Rev. Geophys.*, *52*, 33–76, doi:10.1002/2012RG000419.
- Powers, J. G. (1997), Numerical model simulation of a mesoscale gravity wave event: Sensitivity tests and spectral analysis, *Mon. Weather Rev.*, *124*, 1838–1869.
- Reeder, M. J., and M. Griffiths (1996), Stratospheric inertia-gravity waves generated in a numerical model of frontogenesis. Part II: Wave sources, generation mechanisms and momentum fluxes, *Q. J. R. Meteorol. Soc.*, *122*, 1175–1195.
- Rossby, C. G. (1938), On the mutual adjustment of pressure and velocity distributions in certain simple current systems, *ii. J. Mar. Res.*, *2*, 239–263.
- Simmons, A. J., and B. J. Hoskins (1978), The life cycles of some nonlinear baroclinic waves, *J. Atmos. Sci.*, *35*, 414–432.
- Skamarock, W., J. B. Klemp, J. Dudhia, D. O. Gill, D. Barker, M. G. Duda, X.-Y. Huang, and W. Wang, (2008), A description of the advanced research WRF version 3. NCAR Technical Note NCAR/TN-475+STR, 113 pp., doi:10.5065/D68S4MVH. [Available at <http://opensky.library.ucar.edu/collections/TECH-NOTE-000-000-000-855>]
- Snyder, C., W. Skamarock, and R. Rotunno (1993), Frontal dynamics near and following frontal collapse, *J. Atmos. Sci.*, *50*(18), 3194–3211.
- Snyder, C., D. J. Muraki, R. Plougonven, and F. Zhang (2007), Inertia-gravity waves generated within a dipole vortex, *J. Atmos. Sci.*, *64*, 4417–4431.
- Snyder, C., R. Plougonven, and D. Muraki (2009), Mechanisms for spontaneous gravity-wave generation within a dipole vortex, *J. Atmos. Sci.*, *66*, 3464–3478.
- Tan, Z., F. Zhang, R. Rotunno, and C. Snyder (2004), Mesoscale predictability of moist baroclinic waves: Experiments with parameterized convection, *J. Atmos. Sci.*, *61*, 1794–1804.
- Tan, Z., F. Zhang, R. Rotunno, and C. Snyder (2008), Corrigendum for Tan et al. (2004), *J. Atmos. Sci.*, *65*, 1479–1479.
- Uccellini, L. W., and S. E. Koch (1987), The synoptic setting and possible source mechanisms for mesoscale gravity wave events, *Mon. Weather Rev.*, *115*, 721–729.
- Wang, S., and F. Zhang (2007), Sensitivity of mesoscale gravity waves to the baroclinicity of jet-front systems, *Mon. Weather Rev.*, *135*, 670–688.
- Wang, S., and F. Zhang (2010), Source of gravity waves within a vortex-dipole jet revealed by a linear model, *J. Atmos. Sci.*, *67*, 1438–1455.
- Wang, S., F. Zhang, and C. Snyder (2009), Generation and propagation of inertia gravity waves from vortex dipoles and jets, *J. Atmos. Sci.*, *66*, 1294–1314.
- Wang, S., F. Zhang, and C. C. Epifanio (2010), Forced gravity wave response near the jet exit region in a linear model, *Q. J. R. Meteorol. Soc.*, *136*, 1773–1787.
- Wei, J., and F. Zhang (2014), Mesoscale gravity waves in moist baroclinic jet-front systems, *J. Atmos. Sci.*, *71*, 929–952, doi:10.1175/JAS-D-13-0171.1.
- Wu, D. L., and F. Zhang (2004), A study of mesoscale gravity waves over the North Atlantic with satellite observations and a mesoscale model, *J. Geophys. Res.*, *109*, D22104, doi:10.1029/2004JD005090.
- Zhang, D. L., and J. M. Fritsch (1988), Numerical simulation of the meso-beta scale structure and evolution of the 1977 Johnstown flood. Part III: Inertia-gravity waves and the squall line, *J. Atmos. Sci.*, *45*, 1252–1268.
- Zhang, F. (2004), Generation of mesoscale gravity waves in the upper-tropospheric jet-front systems, *J. Atmos. Sci.*, *61*, 440–457.
- Zhang, F., and S. E. Koch (2000), Numerical simulation of a gravity wave event over CCOPE. Part II: Wave generated by an orographic density current, *Mon. Weather Rev.*, *128*, 2777–2796.
- Zhang, F., S. E. Koch, C. A. Davis, and M. L. Kaplan (2001), Wavelet analysis and the governing dynamics of a large-amplitude gravity wave event along the east coast of the United States, *Q. J. R. Meteorol. Soc.*, *127*, 2209–2245.
- Zhang, F., S. E. Koch, and M. L. Kaplan (2003), Numerical simulations of a large-amplitude gravity wave event, *Meteorol. Atmos. Phys.*, *84*, 199–216.
- Zhang, F., N. Bei, R. Rotunno, C. Snyder, and C. C. Epifanio (2007), Mesoscale predictability of moist baroclinic waves: Convection-permitting experiments and multistage error growth dynamics, *J. Atmos. Sci.*, *64*, 3579–3594.
- Zhang, F., M. Zhang, J. Wei, and S. Wang (2013), Month-long simulations of gravity waves over North America and North Atlantic in comparison with satellite observations, *Acta Meteorol. Sin.*, *27*, 446–454.